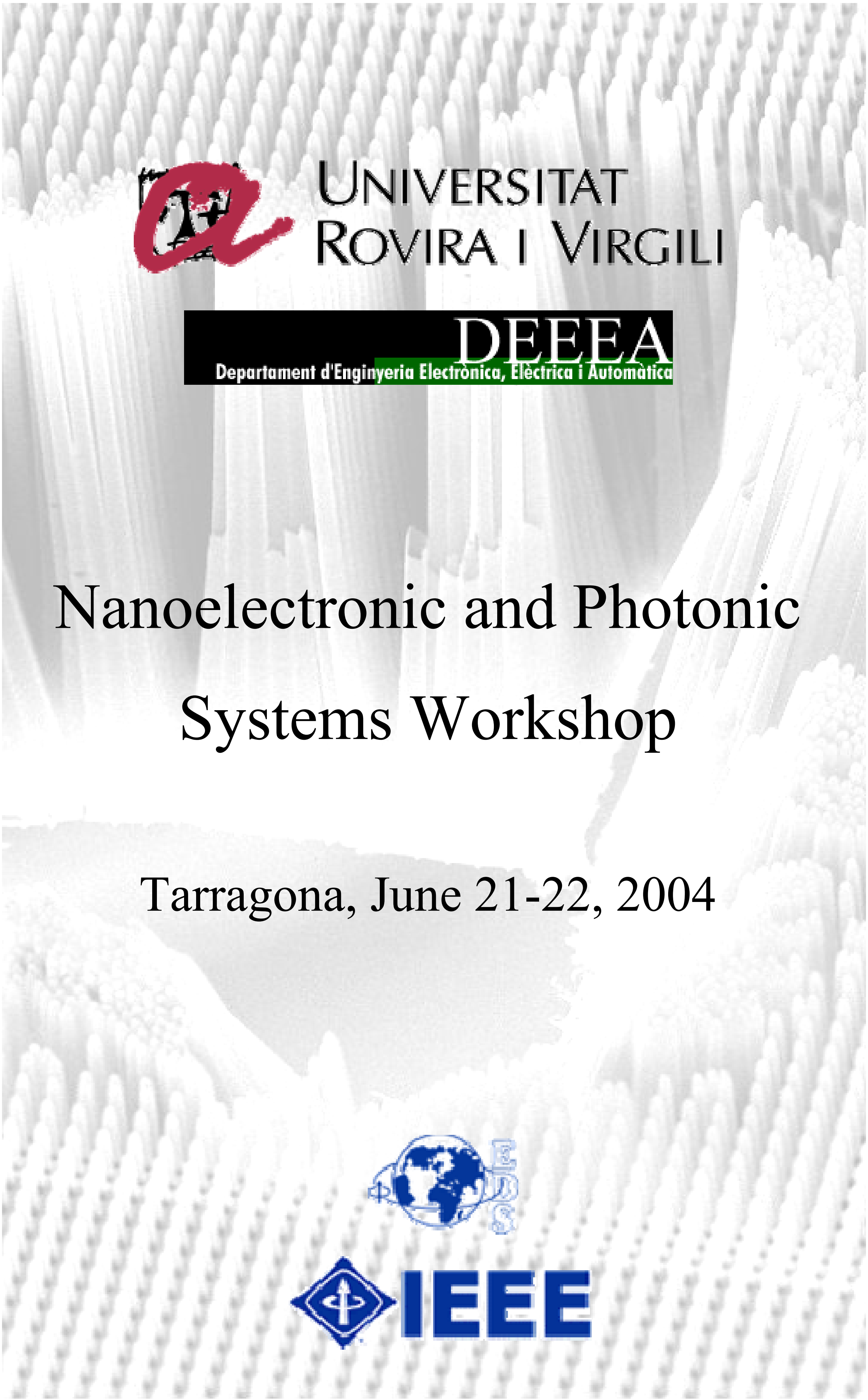

UNIVERSITAT
ROVIRA I VIRGILI

DEEEA
Departament d'Enginyeria Electrònica, Elèctrica i Automàtica

Nanoelectronic and Photonic Systems Workshop

Tarragona, June 21-22, 2004

EDS

IEEE

Abstracts Book

Nanoelectronic and Photonic Systems Workshop

Tarragona, June 21-22, 2004

Organising Comitee

Josep Pallares Marzal

Lluis F. Marsal Garvi

Josep Ferré Borrull

Anna Beltran Ras

Margarita Rebenaque Esteve

Schedule

Monday, 21th June

10:00 Opening session

10:15 Plenary session 1

11:30 Coffee break

11:45 Plenary session 2

13:00 Lunch

15:00 Poster session

16:30 Plenary session 3

17:45 Coffee break

Tuesday, 22th June

10:15 Plenary session 4

11:30 Coffee break

11:45 Plenary session 5

13:00 Lunch

15:00 Poster session

16:30 Plenary session 6

17:45 Coffee break

18:00 Closing sesion

Invited Speakers

Plenary sesion 1

Sensors, Actuators and Microsystems

Prof. Nico de Rooij

SAMLAB, Institute of Microtechnology,
University of Neuchatel, Switzerland

Plenary sesion 2

Noise measurements and information in nano-particle tungsten oxide based gas sensors

Prof. P. Heszler

Angstrom Laboratory, Uppsala University, Sweden

Plenary sesion 3

MOS RF Noise Modeling and Design of Low Noise RFICs

Prof. Jamal Deen (Distinguished Lecturer IEEE)

McMaster University, Hamilton, Canada

Plenary sesion 4

Macroporous Silicon for 3D Photonic Crystals in the IR

Prof. F. Müller

Max-Plank-Institut für Mikrostrukturphysik, Halle, Germany

Plenary sesion 5

Magneto-Photonic Crystal Tunable Filters

Prof. F. Jonsson

NMRC, Photonic Nanostructures Group, Cork, Ireland

Plenary sesion 6

Photonic Crystals and Left-Handed Materials

Prof. M. Kafesaki

IESL-FORTH, Crete, Greece

Index

The Dependence of Output Current Response on Materials of Chemical Sensors Working Electrodes

Martin ADÁMEK[1], Jan PRÁŠEK[1], Edgar SOTTER[2]

1. Dept. of Microelectronics, Technical University of Brno, Údolní 53, 602 00 BRNO, Czech Republic.
Tel.: +420 541 146 136, Fax: +420 541 146 298, E-mail: prasek@feec.vutbr.cz
2. Dept. Enginyeria Electrònica Elèctrica i Automàtica, Universitat Rovira i Virgili, Avd. Països Catalan, 26,
43007 Tarrragona, Spain

Abstract

Miniature electrochemical sensors can be produced by thick film technology (TFT) [1]. Production technology optimization of thick film sensors, the adjustment of optimal technological properties and especially the optimal properties of thick film electrode materials are main problems of sensor design [2]. The comparison of working electrode materials for TFT chemical sensor is discussed in this paper. Measurements were done on thick film amperometric sensor, which is produced by BVT Technologies, a.s. [3]. All measurements were done using a standard electrochemical couple of potassium ferrocyanide-ferricyanide.

1. Introduction

At the beginning, the thick film technology was focused on production of integrated circuits. The basic use of TFT was in the production of small series of non-standards integrated circuits, special integrated circuits and prototypes. Nowadays, the use of TFT is evolved to the area of nonconventional applications, e.g. heating elements for pots, displays, antennas for chip cards, fuses and especially the sensor systems. TFT chemical sensors are cheap, sufficiently sensitive and accurate, with good mechanical and electrical properties.

2. The processes on the TFT electrodes

Processes on electrodes of TFT electrochemical sensors are more complicated than in classical electrochemistry. The materials of TFT electrodes are non-homogeneous from microscopic point of view (composition, structure...), they do not have well defined area, roughness of surface, etc.
The active area is bigger than the effective geometric area. Complicated geometric area can be an advantage or disadvantage depending on the measuring process. The smaller physical area is good for immunosensors whereas larger physical area is extremely important in case of immobilization of enzymes i.e. enzyme biosensors. During the technological process the surface oxide layer grows on active layer. It means that the electrochemistry of TFT electrochemical sensors can't be understand as pure metal electrode but it must be considered as metal-metal oxide electrodes. The classical metal electrodes are irreproducible chemically oxidized during their function. The structure of electrochemically deposited layers of oxides differs from layers of thermally prepared oxides. It means that in certain circumstances the TFT electrochemical electrodes have more reproducible and stable response.

3. The practical measurements

1.

2. 3.1. Chemicals

Basic electrochemical solution of a 0,1 mol.l^{-1} potassium ferrocyanide $K_4Fe(CN_6)$ and 0,1 mol.l^{-1} potassium ferricyanide $K_3Fe(CN_6)$ and 0,4 mol.l^{-1} KOH was prepared and used for measurement. All chemicals were of high purity and used as received.

3. 3.2. Description of workplace

The base of workplace is analytical chemical workstation AEW2 – 10 (Sycopel Scientific, UK). The instrument is a potentiostat for various electrochemical methods measuring - Open circuit, Potentiostatic, Galvanostatic, Potentiodynamic, Galvanodynamic, Pulse amperometric etc. [4]. The workstation is controlled by computer. The computer gathers and draws a measured data that can be exported into Microsoft Excel that enables other data processing and presentation.

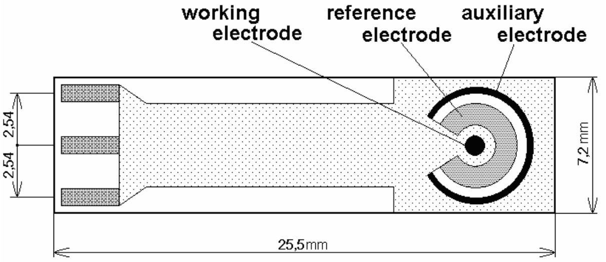

Fig.1. Standard TFT amperometric sensor [3].

The practical measurements were done in a glass electrochemical cell. In the cell there were Ag/AgCl reference electrode and measured sensor (fig. 1.) putted in 5 ml of standard reversible system solution mentioned in subsection 3.1.

4. 3.3. The description of TFT sensor

Standard TFT amperometric sensors (fig. 1.) deposited on Al_2O_3 substrate (BVT Technologies, Czech Republic) [3] were used for measurements. The materials of electrode for individual type of sensors are showed in table 1. This type of amperometric sensors is usually used as the sensor for basic electrochemical measurement, e.g. for H_2O_2, glucose, ferricyanide, pesticide determine and for enzymes deposition. Complete sensors datasheets can be found in [3].

Type of Sensor	Electrode Material		
	Working	Reference	Auxiliary
AC1.WS.R1	PtAu (15/85%)	Ag/AgCl (60/40%)	PtAu (15/85%)
AC1.W1.R1	AuPd (98/2%)	Ag/AgCl (60/40%)	AuPd (98/2%)
AC1.W2.R1	Pt (100%)	Ag/AgCl (60/40%)	Pt (100%)
AC1.W3.RS	AgPd (98/2%)	AgPd (98/2%)	AgPd (98/2%)
AC1.W4.R1	C (7101)	Ag/AgCl (60/40%)	PtAu (15/85%)
AC1.W5.R1	C (7105)	Ag/AgCl (60/40%)	PtAu (15/85%)

Table1. The electrode materials of sensors used for measurement.

3.4. Results and discussion

The potentiodynamic method, where a potential between the working electrode and the reference electrode is linearly changed with pre-select scan rate over defined range and corresponding current is measured and recorded, was used for measurements. Measurements were done in the potential range <-1000 mV; +1200 mV>. Examples of some results are shown in fig. 2.

These graphs are showing that:

- The optimal scan rate for measurement is in limit between 10 mV.s^{-1} to 50 mV.s^{-1}.
- The optimal materials of working electrode are sensor types AC1.W2.R1 and AC1.WS.R1.
- Though the redox couple is in the classical electrochemical systems reversible, the behaviour with graphite paste electrode is irreversible.

4. Conclusions

Various standard TFT pastes for working electrodes of amperometric sensor were tested and compared. The practical measurement was made in a model reversible system, alkaline solution mixture of potassium ferricyanide and potassium ferrocyanide. Sensor types AC1.W2.R1 and AC1.WS.R1 are the best types of measured sensors. The optimal scan rate is appeared to be in limit between 10 and 50 mV.s^{-1}. However the reversible electrochemical redox couple was used the output signal was irreversible. The results show that the graphite pastes deposited on standard amperometric sensor have dependence of peaks voltage on various scan rates.

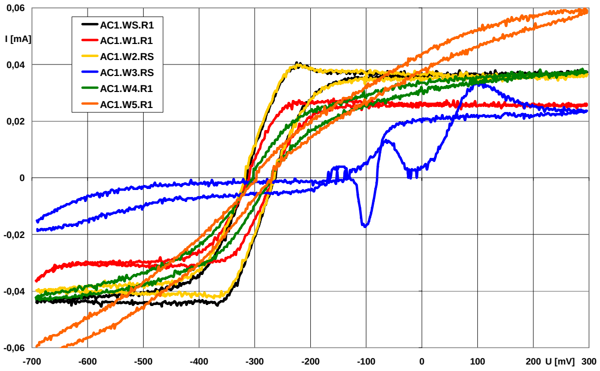

a) Scan rate v = 5 mV.s^{-1}

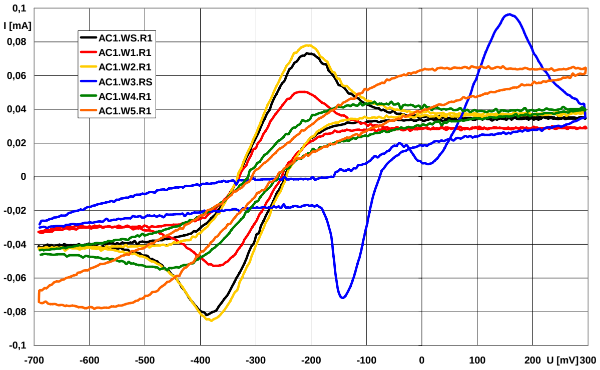

b) Scan rate v = 20 mV.s^{-1}

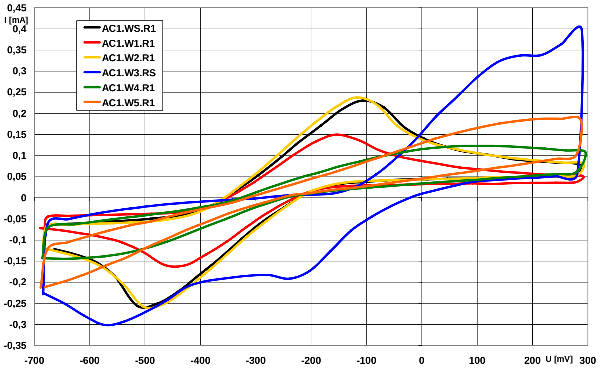

c) Scan rate v = 200 mV.s^{-1}

Fig.2. The dependence of output current response on materials used for working electrodes.

Acknowledgement

The work was partially supported by Czech Ministry of Education in the frame of Research Plan MSM 262200022 MIKROSYT Microelectronic Systems.

References

[1] Hascard, M., Pitt, K.: Thick-film Technology and Applications, Electrochemical Publications LTD, 1997, ISBN 0901150355.
[2] Adamek, M., Krejci, J., Szendiuch, I.: The Dependance of TFT Chemical Sensors on the Technology of Preparation Methods of Testing In Proceedings of 34th IMAPS. Interantional Sympozium. 34th IMAPS Interantional Sympozium. Baltimore, USA: IMAPS USA, 2001, s. 688 - 692, ISBN 0-930815-64-5.
[3] BVT Technologies, a.s., WWW pages, www.bvt.cz
[4] SYCOPEL SCIENTIFIC LIMITED, WWW pages, www.sycopel.com.

Manufacture of a system preconcentrador-matrix of sensors for the detection of low levels of benzene

F. Blanco, X. Vilanova, M. Vinaixa, E. Sotter and X. Correig

Departament d´ Enginyeria Electrònica, Elèctrica i Automàtica, Universitat Rovira i Virgili
Av. dels Països Catalans 26, 43007 Tarragona (Spain)
Tel: 977 558 764, Fax: 977 559 605, E-mail: fblanco@etse.urv.es

Abstract

In this paper appears the research that is being developed to obtain a preconcentrator-sensor-array system to monitor harmful gases at very low concentrations.

1. Introduction

The environmental study needs measurements of pollutants at trace concentrations (ppm to ppt), because even at these levels they suppose a threat to health and to environment [1]. Benzene (C_6H_6) is a polluting gas, that is know since 1895. It is a colorless liquid, very inflammable, of characteristic scent, lighter than the water and insoluble in it. It is perhaps the more studied organic compound, due to its carcinogenic effects and to the high poisoning effects when inhaled in a great amount [2]. The maximum permitted exposure limit for benzene, according to the 2003 norm, is 5 ppb (16.25 μgm^{-3}) [3].

The benzene and its derivatives are included in the known chemical group of aromatic compounds.

For the detection of this type of gases, different techniques has been developed, mainly based in gas chromatography, combined with preconcentrators systems to be able to detect as low concentrations. In the present work we try to extend the use of the preconcentrators to another alternative technique: the use of gas sensors arrays.

The preconcentrators consist in a layer of chemical compound (adsorbent), which can trap the molecules of benzene, and to release them when this is heated.

The final mission is to develop a microsystem that includes a matrix of sensors and a preconcentrator.

2. Experimental development

In order to make the first investigations of adsorbent, Silicone OV-17 has been used (50% phenyl - 50% methyl siloxane) acquired of Supelco [4], and deposited on alumina substrate. This adsorbent, is a polymer with good capacity to trap VOC´s (Volatile Organic Compounds). Their physical and thermal characteristics make them to be very versatile for the manufacture of the preconcentrator.

Fabrication process of preconcentrator

Sample preparation

Firstly, the alumina substrates were cleaned with xylene to eliminate the impurities that may be present at the surface by effects of their manipulation: Later, they are dried before making the deposition of the adsorbent.

Adsorbent deposition

The deposit of the adsorbent (Ov-17) without diluting, it is made by means of Drop-Coating; the more suitable needle is selected to obtain the size of drop that can cover the surface that we wished.

The preliminary tests have been made on alumina substrates and alumina with a platinum resistance, that will be the element for heating the substrate to generate the pulse for thermal desorption.

These preliminary tests must verify the adhesion of this material on these materials, and verify the obtained effective surface of adsorbent.

Drying

Finally, an annealing of the aluminas has been made, at a temperature of 120ºC by 48 hrs to dry the adsorbent.

Sensors

An array of microhotplate sensors has been developed. It consists of four Si_3N_4 membranes. Each sensor has a POCl3-doped polysilicon heating meander which also serves as temperature sensor. Two types of Pt interdigited electrodes with area of 400 µm x 400 µm were designed. Each array has two electrodes with 50 µm gap and two with 100 µm gap. Active layer of SnO_2 has been deposited using RF magnetron sputtering. After this deposition the layer was doped using the same technique. Finally, the sensor was annealed at 400ºC in air for 2 hours. The sensors were diced and packaged (Fig.1). These sensors will be applied to detect the benzene that will be purged from the preconcentrator.

3. Results

The results obtained in the first experiments have shown that the Ov-17 does not present any problem to adhere to alumina, as it's shown in figure 2.

In order to obtain the formation of this layer, it is necessary to deposit a minimum amount of adsorbent. When analyzing the samples by means of SEM

(Scanning Electron Microscopy), we found that the adsorbent is located between pores of alumina, figure 3. Therefore, we have the advantage to have natural channels, through which will pass the gas and the benzene molecules will be trapped. In this figure, the elements that can be observe are Si, Al and Pt. The Si is one of the principal components of the adsorbent. The aluminum appears because the substrate is from alumina and the platinum is due to the Pt electrodes.

4.Conclusions

Being the first stage of our investigation of the preconcentrator, the results obtained indicate that the quantity of the deposited adsorbent was not optimum. That is why, in the future work, we have to deposit several adsorbent layers to ensure the uniformity of this. Finally, the tests with the gases have to be realized, to determine that amount of benzene molecules is trapped and if this amount is suitable be detected with the sensors.

Fig.1. Microhotplate sensors.

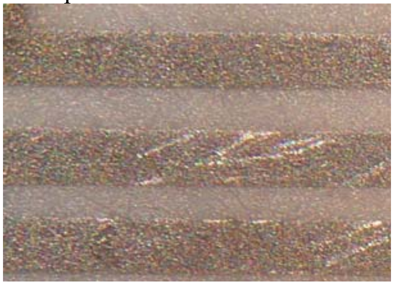

Fig.2. Alumina with platinum resistance, after drying the deposited adsorbent.

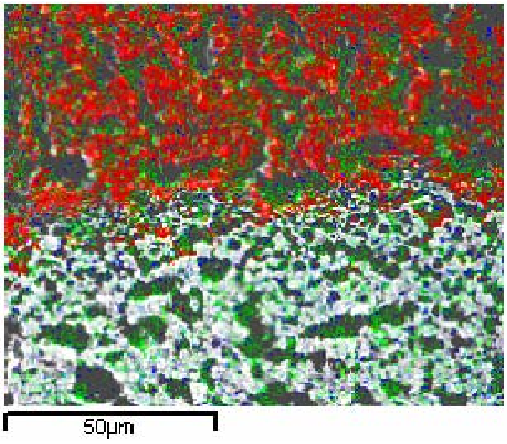

Fig.3. Alumina SEM image (Aluminum=Red, Silicone=Green, Platinum=Blue).

References

[1] Minhee Kim, Somenath Mitra "A microfabricated microconcentrator for sensors and gas chromatography" Journal of Chromatography A. 996 (2003) 1-11.

[2] Quimica del Benceno
http://132.248.56.130/qo1/Mo-cap13.htm

[3] Mohammed Mabrook, Peter Hawkins "A rapidly responding sensor for benzene, metanol and etanol vapours based on films of titanium dioxide dispred in a polymer operating at room temperature" University of West of England
Sensors and Actuators B 75 (2001) 197-20

[4] Sigma-Aldrich "Material safety date sheet of silicone OV-17" (2004)
https://www.sigmaaldrich.com/cgi-bin/hsrun/Suite7/Suite/HAHTpage/Suite.HsViewHierarchy.run

Concatenation of a Fuzzy Artmap neural network to different variable selection techniques to enhance E-nose performance

C. Durán[1, 2], J.Brezmes[1], O.Gualdrón [1, 2], M.Vinaixa[1], E.Llobet[1], X.Vilanova[1], X.Correig[1]
[1]Departament d'Enginyeria Electrònica, Elèctrica i Automàtica, ETSE, Universitat Rovira i Virgili,
Avda. Països Catalans, 26, 43007 Tarragona, España
[2]Departament of Electronic Engineering, University of Pamplona, Km 2, Pamplona, Colombia

Abstract

This work compares the coupling of different variable selection techniques to a Fuzzy Artmap neural network in order to enhance Electronic Nose performance. The study was applied to the classification of 7 fungal species, boosting classification performance from 43% to a 75% using the combination of DFA and Fuzzy Artmap.

1. Introduction

Many microbial problems in bakery products are produced by fungal infections. The growth of these micro-organisms in bakery products during storage are specially important in three different genres: *Eurotium*, *Aspergillus* and *Penicillium,* [1].
The goal of this paper is to improve the performance of an electronic nose in the classification of seven fungal species coupling a Fuzzy Artmap neural network to different variable selection techniques [2, 3].

2. Experimental

2.1. Materials and methods

An application specific electronic nose was built using 12 metal oxide commercial gas sensors, (FIS SP-series and TGS 8-series). A Headspace Autosampler (Hewlett Packard 7694) was used to heat each vial and the volatiles emitted were driven to the sensor chamber.
Sensor responses were acquired through a PCI-NI6023E data-acquisition card via PC. The control of the hardware, sampling equipment and data acquisition was done using written-in-house software under Matlab 6.1. Pattern recognition was performed using Fuzzy Artmap coupled to different variable selection techniques based on PCA, DFA, Genetic Algorithms (GAs), Forward selection and intra/inter variance criteria.

Genres	Replicates
Eurotium Repens	2
Eurotium Herbariorum	2
Eurotium Amstelodami	2
Eurotium Rubrum	2
Aspergillus flavus	2
Aspergillus Niger	2
Penicillium Corylophilum	2
Cultivation Mid	2

Table 1. *Fungal Species measured*

2.2. Sample preparation

A total of 16 vials (20 ml) were prepared. 14 contained 2 replicates of 7 fungal species and 2 contained empty cultivation mids (substance to cultivate fungi). Finally, 3 vials of ethanol were used for sensor calibration. Table 1 shows the seven different species measured. Note that each shadow denotes a different fungal genre.

3. Results and discussion

As mentioned earlier, measured data was processed coupling Fuzzy Artmap neural networks to different variable selection approaches. In all cases, a leave-one-out approach was used.
This iterative validation procedure generates N evaluation procedures (1 for each measurement). In each iteration, a different measurement is left out, while the remaining ones are used to build the model (PCA, DFA, etc) and train the network.
The remaining measurement (the one not used for training) is then projected onto the model and classified using the already trained network. This is repeated N times (one for each measurement) so that the final result is the average success of the entire iterative process.

3.1. Fuzzy Artmap classifier

First, in order to compare results, a Fuzzy Artmap neural network was used to classify the samples from 8 fungal using all the sensors (12 variables). The classification success rate into seven categories reached a 43 %.
Once this classification was obtained, the goal was to couple different variable selection techniques to the fuzzy paradigm to see whether this approach improved results.

3.2. Using DFA as a variable selection technique

In each iteration, a DFA model was built with the training measurements. Then, the coordinates of the training samples in the DFA projection were used to train a Fuzzy Artmap neural network. The evaluation measurement was projected onto the DFA and the coordinates fed to the neural network. Eigenvectors (the coefficients for canonical variables) were used to classify samples.
A 75% success rate was achieved using only 2 eigenvectors. These results were expected due to the

clusters of fungal genres that the DFA graphic shows in figure 1. It has to be noted that, since DFA is a supervised method, overfitting results can be obtained in the training measurement set. Anyway, when using a cross validation method, the overfitting risk is eliminated since the evaluation measurement has not been used to build the DFA model.

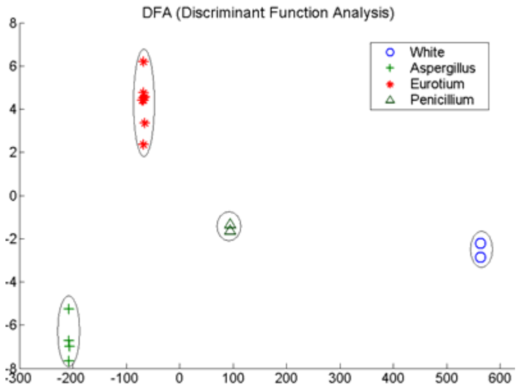

Fig.1. DFA clustering of fungal genres.

3.3. PCA used as a variable selection method coupled to Fuzzy Artmap

In each iteration, a PCA model was calculated with the training measurements and the coordinates fed to a fuzzy Artmap for training purposes; then, with the PCs calculated and the weights from the Fuzzy Artmap, the validation measurement was projected and evaluated. Results with different number of principal components were tested. Best results were achieved with just 2 PC's, where a classification rate of 63 % was achieved.

3.4. Results coupling Genetic Algorithms and Fuzzy Artmap:

The GA coupled to the Fuzzy Artmap classifier selected 5 out of 12 variables. The fitness was evaluated as the PER (Predictor Error Rate) and the cross-validation of order one with 16 measurements was applied. The PER was 0.3556 and the algorithm converged after 33 generations. The success rate was 63 %.

3.5. Variable selection using intra/inter variance

A variance criterion was defined in order to reduce the number of variables. Equation 1 shows this criteria, which somehow measures the resolution of each variable related to the differentiation between the 8 fungal species. *External variance* was calculated as the variance between the 8 average (centroid) values obtained for each fungal sample (plus blank vials). *Internal variance* was defined as the average of the 8 distances calculated for the 2 repetitions performed on each sample. A higher value for Vr means a better resolution capability for a given variable.

$$Vr = \frac{ExternalVariance}{InternalVariance} \qquad (1)$$

Fuzzy ARTMAP was applied to evaluate the selection. Best results where obtained when selecting the 7 variables with the highest Vr. The success rate topped at 63 %.

3.6. Forward selection

The forward selection algorithm used in linear regression was applied in our case to select a subset of the 12 original variables. In the end, only 2 variables were selected. These variables were used as the input to a Fuzzy Artmap model The neural model was cross-validated using 16 measurements. The success rate achieved was 70 % with the selected variables.

4. Conclusions

Table 2 summarises the results obtained, comparing the coupling of different variable selection techniques to a Fuzzy Artmap. The number of variables that give best results is also specified. We can observe that applying any of the methods leads to better results than using the Fuzzy Artmap alone. The best results were obtained coupling DFA to a Fuzzy Artmap neural network using only 2 variables (factors) instead of 12.

Methods	**Results**	**Subset selected**
Fuzzy ARTMAP alone	43%	12
DFA+ Fuzzy ARTMAP	75%	2
PCA+ Fuzzy ARTMAP	63%	2
GA+ Fuzzy ARTMAP	63%	5
Variance Criterion	63%	7
Forward + Fuzzy ARTMAP	70%	2

Table 2. Variables selected.

As it can be seen the forward selection method gives very good results and the variables selected come from the original sensor array, giving a straightforward interpretation (sensor selection) that can be used to reduce the sensor array for a given application. That is why this method should be studied in greater detail.

Acknowledgments

This work was funded by redes de centros en metabolismo y nutrición, C03/08".

References

[1] N. Magan et al., *J. of Stored Prod.* 36, (2000), pp: 319-340.
[2] J. Brezmes et al., *ISOEN Rome*, (2002), pp: 224-227.
[3] A.J. Miller et al., London; (1990).

Micro-hotplate gas sensors based on functionalized carbon nanotube films

E.H. Espinosa, R. Ionescu, E. Sotter, E. Llobet, A. Felten*, C. Bittencourt*, J.J. Pireaux*

Dept. Enginyeria Electrònica, Universitat Rovira i Virgili,Avd. Països Catalans 26, 43007 Tarragona (Spain),
Phone: +34 977 558502, Fax: +34 977 559605,E-mail: ellobet@etse.urv.es
*LISE, Facultés Universitaires Notre Dame de la Paix, B-5000 Namur, Belgium

Abstract

Differently functionalised multi-wall carbon nanotubes (MWNT) were deposited onto microhotplate gas sensor substrates by the drop coating method. A well-adhered thick film of carbon nanotubes mesh (~ 17 µm) was obtained after annealing in air at different temperatures. Gas sensing properties were investigated for NO2, and NH3. These species can be detected at room temperature.

1. Introduction

Carbon nanotubes (CNTs) represent a recently employed material to form the active layer of semiconductor gas sensors. Two general categories of CNT can be fabricated [1], specifically single-wall carbon nanotubes (SWNTs), which are a cylinder rolled from a graphitic sheet, and multi-wall carbon nanotubes (MWNTs), which are a coaxial structure of various graphitic cylinders of different diameters.

CNTs result advantageous for gas sensing because of their larger surface area [2]. Another important property is that they are sensitive to gases at low temperatures (e.g. below 200 ºC), and also at room temperature [3], which reduces the power consumption of the device and enables the safe detection of flammable gases. However the presence of a thick graphite-like layer at the surface of the nanotubes, which contributes with sp^2 electronic states, can rule out the sensing potentiality of this material. Several methods, such as chemical, electrochemical and plasma treatment can be applied to modify the chemical composition of the nanotubes surface [4, 5].

In this work we applied the drop coating method for depositing thick films of CNTs onto micro-hotplate substrates. The nanotubes were previously treated in oxygen plasma, what reduced the amount of graphite at the surface.

2. MWNT deposition

Four differently funtionalised MWNTs (Nanocyl ®) were used to form the sensitive layer of micro-hotplate gas sensors (substrates provided by the CNM, Barcelona, Spain). Depending on the oxygen plasma parameters the excited species, radicals, electrons, ions and UV light within the plasma interact with the surface of the CNT breaking the C-C bonds and creating active sites for bonding of functional groups. By doing so, it is possible to reduce the graphite-like layer at a point that the catalysts used in the fabrication of the nanotubes are exposed. XPS analyses were performed in order to evaluate the chemical change at the CNT surface. Specifically, they were 4 different types:

- A: Not funtionalised MWNTs
- B: MWNTs with 10at.% oxygen at the surface
- C: MWNTs with 20at.% oxygen at the surface
- D: MWNTs with 20at.% oxygen +Co +Fe + Al

The MWNTs were near 50 µm long, their inner diameters ranged between 2 and 7 nm, their outer diameters between 3 and 15 nm.

A drop coating method was employed for the deposition of CNTs onto the sensor substrates [6].

The depositing paste was prepared dispersing MWNTs in glycerol (25 µg in 1 ml). The paste was drop-coated using a micro-injector (JBE1113 Dispenser, I&J FISNAR Inc., USA). The as-deposited films were annealed in situ at three different temperatures (350, 400 and 480 ºC) for 2 hours. 24 sensors were prepared in total (2 replicates × 4 materials × 3 annealing temperatures). The sensors' baseline resistances after annealing ranged typically between 50 and 150 Ω. Figure 1 shows a picture of a four-element micro-hotplate sensor mounted on a standard TO-8 support, where the CNTs thick film lay over the micromachined membranes.

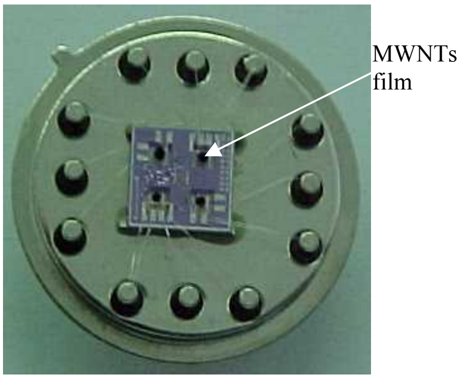

Fig. 1. 4-element micro-array of drop-coated MWNTs

A scanning electron microscopy (SEM) image of the MWNTs film is shown in Figure 2. The formation of a dispersed mesh of MWNTs can be observed. SEM analyses showed that well-adhered thick films of MWNTs were obtained, which had an average thickness of about 17 µm. All these results indicate a correct deposition of the sensing material.

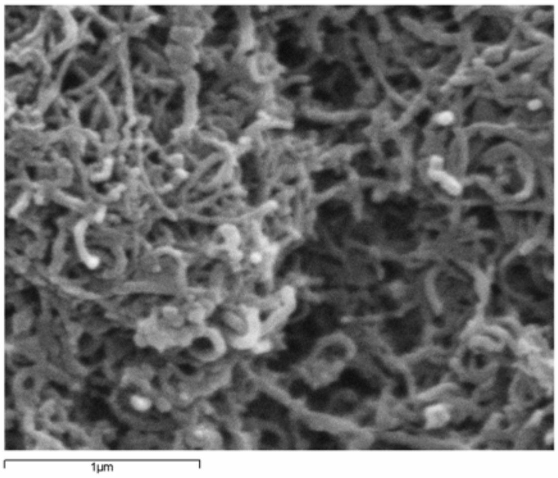

Fig. 2. SEM image of the MWNTs film deposited over the sensor electrodes

3. Room temperature detection of NO_2 and NH_3

The performances of the sensors were tested for different concentrations of NO_2 (500 ppb, 1, 5 and 10 ppm) and NH_3 (200, 500 and 1000 ppm) at ambient temperature. For conducting the experiments, two four-element MWNTs sensors were kept into a 30 ml test chamber. A continuous flow measurement system, with a constant flow rate of 0.2 l/min, was used to generate the desired concentrations of NO_2 and CO in dry air (79% N_2 and 21% O_2). The sensor resistances were acquired and stored in a PC using an Agilent 34970A data acquisition unit. Figures 3 and 4 show sensor resistance after exposure to increasing concentrations of NO_2 and NH_3. The best responses to NO_2 were obtained by sensors coated with films types B and C annealed at 350ºC (operated at room temperature). These correspond to the MWNT functionalised with oxygen. On the other hand, the best sensitivity to NH_3 was obtained by the sensor with the active layer made from material D and annealed at 480ºC. The traces of catalytically active metals present in D samples play an active role in the detection of ammonia.

4. Conclusions

Detection of NO_2 and NH_3 concentrations as little as 500 ppb and 200 ppm, respectively, was found to be possible at ambient temperature with MWNTs-based gas sensors fabricated by drop coating. The presence of the metallic catalysts used in the preparation of the CNTs at their surface proved to play an important role in selectivity.

Plasma treatment showed to improve the sensing potentiality of CNTs by reducing the thickness of the graphite-like layer at their surface. However low sensor resistance is still present, which is probably linked with graphite-like species. We expect that combining a chemical purification process with plasma functionalization of the MWNTs will improve results.

Work is in progress for testing sensor responses to other hazardous gases (*e.g.*, CO). Sensitivity to CO is obtained if the operating temperature is raised above ambient temperature.

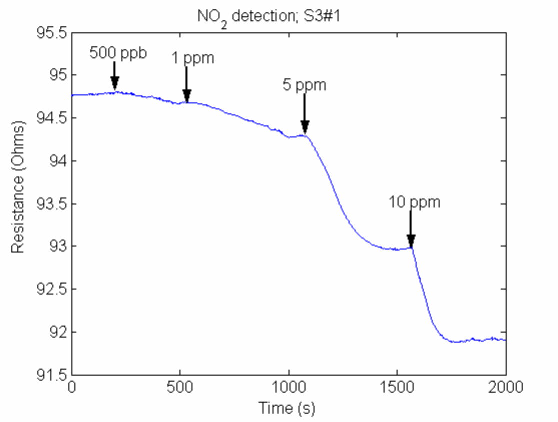

Fig. 3. MWNTs (Material C) sensor response to increasing concentrations of NO_2

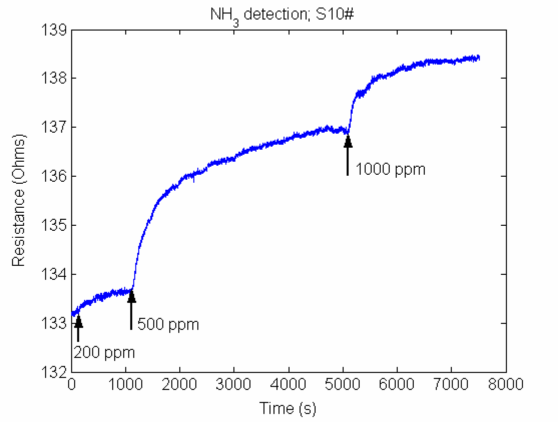

Fig. 4. MWNTs (Material D) sensor response to increasing concentrations of NH_3

References

[1] L. Valentini et al, Mat. Sci. & Eng. C, 23 (2003), pp. 523-529.
[2] O.K. Varghese et al, Sens. and Actuat. B, 81 (2001), pp. 32-41.
[3] S. Peng et al, 3rd Intern. Workshop on Struct. Health Monit., (2001), pp. 1-8.
[4] H. Bubert et al., Diamond and Related Materials, 12 (2003), pp. 811-815
[5] N.O.V. Plank et al., Appl. Phys. Lett 83 (2003), pp 2426-2428
[6] J. LI et al, Nano Lett., 3 (2003), pp. 929-933.

A Synthesizable Multiplication Model for Elliptic Curves in $Z_{239}[x]/(x^{17}-2)$

G. Forte, J.P. Deschamps

Departament d’Enginyeria Electrònica, Elèctrica i Automàtica, ETSE, Universitat Rovira i Virgili, 43007 Tarragona
Phone: 977 558764; Fax: 977 559605; e-mail: fortesagt@yahoo.com

Abstract

The Elliptic Curve Cryptography basically consists of additions, subtractions, multiplications and inversions in a finite field. While the additions and subtractions are easily implemented, the multiplication requires a more elaborated process. The design of a Polynomial Multiplication model into a programmable device is a task that requires compromise between computation time and size of circuit. This paper focuses specifically in the elaboration and results of this circuit.

1. Introduction

Today there is a wide range of distributed systems, which use communication resources that can not be safeguarded against eavesdropping of unauthorized data alteration. Thus cryptographic protocols are applied to these systems in order to prevent information extraction or to detect data manipulation by unauthorized parties.

In 1985, N. Koblitz [1] and V. Miller [2] suggested that elliptic curves could be used for cryptographic public key schemes, but at that time it was very difficult to perform the necessary calculations. Actually, ECC is widely used in cryptographic systems, and all the calculations are done by a computer. But for many portable applications, like smart-cards, cell-phones and others where security is also needed, the most convenient solution is to incorporate the cryptosystem within its circuitry. This can be done by creating a synthesizable cryptography model, written in a description language, which can be programmed in a FPGA or any other programmable device easily adaptable to the main circuitry.

The ECC consists basically in operations using the addition, subtraction, multiplication and inversion in a finite field of characteristic 2 and extension degree in *n*, using polynomial bases. A model is proposed for calculating the polynomial multiplication of order 16 and modulo *n*=239. The finality of this paper is not to demonstrate ECC arithmetic (there are many books and articles related to the topic [3], [4]), but show how the model is designed and can be easily implemented into a system.

2. Multiplication in $Z_{239}[x]/(x^{17}-2)$

Consider three polynomials

$$a(x) = a_0 + a_1.x + a_2.x^2 + ... + a_{16}.x^{16},$$
$$b(x) = b_0 + b_1.x + b_2.x^2 + ... + b_{16}.x^{16},$$
$$f(x) = -2 + x^{17},$$

whose coefficients a_i and b_i belong to Z_p, being $p=239$ a prime number. A circuit that computes $z=a\cdot b \bmod f$ is show in Fig.1

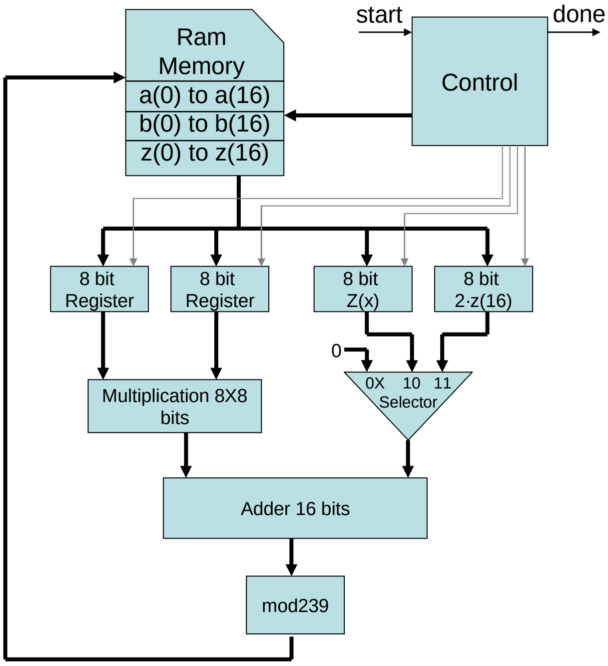

Fig. 1 Polynomial Multiplication Circuit

The control block is the principal part of the circuit, and controls the other components. The polynomials a(x) and b(x) are stored in the RAM memory. A start signal is applied, and the control unit starts the calculation. The required contents of the RAM are stored temporary into 8 bit registers. The operation 2 by the component sixteen of “z” is also required. It multiplies each component of “a” by the whole “b” polynomial then adds the last same degree multiplication stored temporary in “z” and stores it again the memory again. For example, to calculate the first z(16); a(16), b(16) and z(15) are stored in the registers. The circuit multiplies a(16) and b(16). The selector chooses z(15), which in this case is ‘0’ because no multiplication has been done since now. The adder sends its result to the modulus 239 circuit, and this sends its result to the RAM memory again. The control unit only needs a "start" signal, and it will give the "done" signal when finished. The polynomials are always stored and operated in the memory, so there is no extra cost in FPGA area. The counterpart of this is that reading and writing to RAM memory requires more clock cycles.

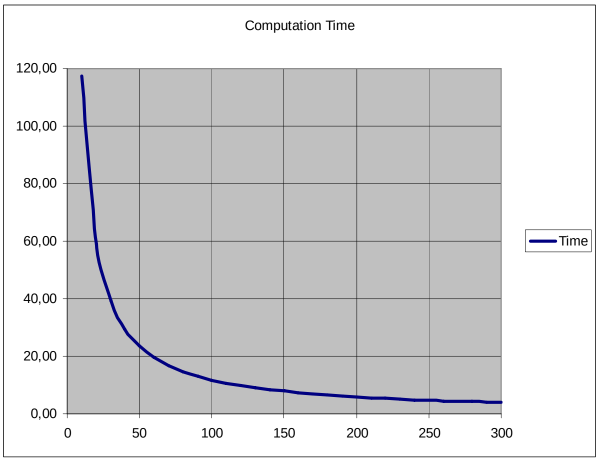

Fig. 2 Time for multiplication depending of the clock frequency

3. Results

This model was implemented in VHDL code. Using a 50 MHz. clock, the total time required to calculate the multiplication is approximately 23.5 µs. The required time is inversely proportional to the frequency, so we get the following equation, plotted in Fig. 2:

$$\text{Time} = \frac{50\ \text{MHz} \cdot 23.5\ \mu\text{s}}{\text{Clock Frequency}}$$

The model was also synthesized for a Xilinx FPGA, the
Spartan 2 model 2s100tq144-6, and the Table 1 were obtained.

Component	Used from total	% used
Number of Slices:	171 out of 1200	14%
Number of Slice Flip Flops:	90 out of 2400	3%
Number of 4 input LUTs:	297 out of 2400	12%
Number of bonded IOBs:	9 out of 96	9%
Number of BRAMs:	1 out of 10	10%

Table 1: Multiplication circuit usage in the Spartan 2s100tq144-6

4. Conclusions

The proposed Polynomial multiplication model has a good time of calculation (23.5 µs at 50 MHz clock) and the space occupied into the FPGA is very low, so it is an efficient one.
This model can be easily adapted to a general circuit, because it uses the data stored in the RAM memory, and only uses two control signals: start and done.

References

[1] N. Koblitz, "Elliptic Curve Cryptosystems", Mathematics of Computation, vol. 48, pp. 203-209, 1987.
[2] V. Miller, "Use of elliptic curves in cryptography", Advances in Cryptology, Proc. CRYPTO'85, LNCS 218, H.C. Williams, Ed., Springer-Verlag, pp. 417-426, 1986.
[3] I. Blake, G. Seroussi and N. Smart, "Elliptic Curves in Cryptography", London Mathematical Society Lecture Note Series 265, 1999.
[4] M. Rosing, "Implementing Elliptic Curve Cryptography", Manning 1999.

LOW LOSS SILICA WAVEGUIDES CONTAINING Si NANOCRYSTALS

C. García, B. Garrido, P. Pellegrino, M. Perálvarez, Y.Lebour, J.A. Moreno, M. López, J.R. Morante
EME, Departament d'Electrònica, Universitat de Barcelona (Spain)

N. Daldosso, M. Melchiorri, L. Pavesi
INFM e Dipartimento di Fisica, Università di Trento, Povo (Italy)

E.Scheid, G. Sarrabayrouse
Laboratoire d'Analysie et d'Architecture des Systèmes (LAAS-C.N.R.S)., Toulouse (France)

We present a thorough study on the optical and structural properties of rib-loaded silica waveguides containing Si nanocrystals, including optical losses measurements. A quadruple implan-tation of Si ions was performed into a thermally-grown SiO_2 layer. The thickness of the resulting flat-profile active region (monitored by Secondary Ion Microscopy) was about 350 nm, with Si excess ranging from 7% to 13%. Complete phase separation and nanocrystal formation was assured by annealing at 1100ºC, and corroborated by Raman measurements. Grain size distribution was determined by EFTEM, with mean values between 3.6 nm and 4.6nm, depending on the Si excess. M-lines spectroscopy was used to determine the refractive index of the active region as a function of the Si excess. All samples showed strong photoluminescence when excited with a He-Cd laser (λ_{exc}=325nm).

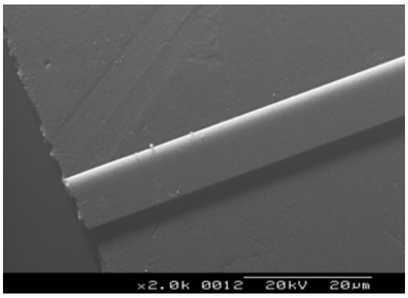

Fig.1. SEM image of an 8μm-wide waveguide

The rib-loaded structure of the waveguides was fabricated on the sample with the 9.5% Si excess, by photolithographic and reactive ion etching processes, with patterned rib widths ranging from 1 to 8 μm. Efficient light propagation in the visible range was observed when end-fire coupling a probe signal into the waveguides, with attenuation losses as low as 11 dB/cm in the red.

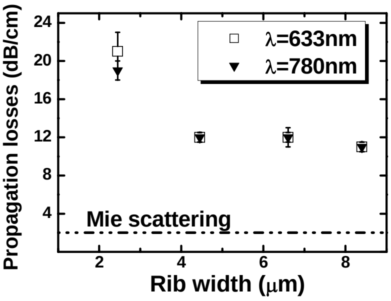

Fig.2. Dependence of the propagation losses with the rib width

The dependence of the losses with the rib width is due to the stronger effect of the wall roughness for smaller ribs. Asymptotic values of around 2 dB/cm for Mie scattering and of about 9 dB/cm for direct absorption were evaluated, corresponding to an absorption cross-section for the nanocrystals of $\sigma_{abs\ 780}$~$5x10^{-19}$ cm^2 . These numbers are promising for the feasibility of a high performance optical amplifier which makes use of similar optimized structures.

Double Gate MOSFET Compact Model Including Scattering

Hamdy A. Hamid[a], B. Iñíguez[a], D. Jiménez[b], L. F. Marsal[a], and J. Pallarès[a]

[a]Departament d'Enginyeria Electrònica, Elèctrica i Automàtica; Escola Tècnica Superior d'Enginyeria; Universitat Rovira i Virgili; 43007-Tarragona, Spain.
[b]Departament d'Enginyeria Electrònica; Escola Tècnica Superior d'Enginyeria; Universitat Autònoma de Barcelona; 08193-Bellaterra (Barcelona), Spain

Abstract:

This work presents a compact model, which includes scattering, for the silicon quantum well MOSFET. The model is based on the Landauer transmission theory and McKelvey´s flux theory, and is continuous from below to above threshold and from linear to saturation regions. A good agreement with 2-D numerical simulations (nanoMOS) is obtained with our compact model. The effect of backscattering on both the channel conductance and the average velocity near the source end is studied in this work.

1. Introduction

Double gate (DG) MOSFET have emerged as promising devices to extend the scalability of CMOS technology down to the nanoscale range. In order to design and project future nanoscale DG-MOSFETs, accurate compact models are required[1,2]. However, backscattering affects the behavior of DG- MOSFET, even if they are nanoscale. Therefore, backscattering has to be included in a general model. The backscattering coefficient has a value between zero and one, and is a function of both the critical length and the low field momentum relaxation length. In this work, our objective is studying and modelling the backscattering effects on nanoscale DG-MOSFETs, using the flux method originally introduced by McKelvey[4]. The paper is organized as follows. In Section 2, we will explain the formulation of Landauer[3] for the ballistic regime, and rewrite it in the form of the directed fluxes (positive and negative fluxes). In Section 3, we will develop a compact scattering model, based on the ballistic model, presented in Section 2. The proposed model will be compared with two-dimensional (2-D) numerical nonequilibrium Green´s function (NEGF) simulations of the same device. Finally, the summary and conclusions of our model will be provided in Section 4.

2. Ballistic Model

Fig. 1 shows the cross section of the symmetrical DG-MOSFET considered in this work. In order to illustrate the behavior of the compact model we have assumed a DG-MOSFET with gate length of 20 nm and the Si-SiO$_2$ interface parallel to (100) plane. The top and bottom gate oxide thicknesses are t_{ox}=1.5 nm, the Si body thickness t_{si} is taken as 1.5 nm. The same gate voltage V_{GS} is applied to both gates. The channel is undoped, the n$^+$ source and drain are highly doped, 10^{20} cm^{-3}. A low field mobility of 120 cm^2/V-sec will be assumed in the channel. All calculations have been done at room temperature.

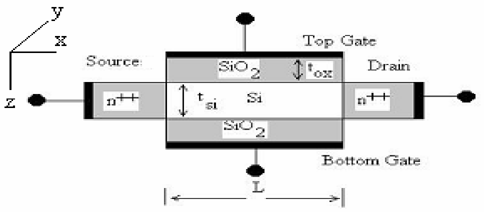

Fig. 1. Cross section of the symmetrical DG-MOSFET considered in this work.

Let us start with the current expression for a quantum wire MOSFET, given by[1]

$$I = \frac{q}{L}\sum_{v}\sum_{k_z,k_y}\sum_{k_x>0} g_v\left(f_S(E) - f_D(E)\right)\left(\frac{\hbar k_x}{m_x^v}\right)T(E) \qquad (1)$$

In this equation, L is the channel length, corresponding to the transport direction (x-direction), and $\hbar k_x / m_x^v$ is the velocity of the electrons as they are injected from the contact with energy E and m_x^v is the effective mass for the transport in the x-direction. If we suppose that the silicon-oxide interface orientation is <100>, then $m_x^1 = m_x^2 = m_T$, $m_x^3 = m_L$, where m_T=0.19m_0 and m_L=0.91m_0, being m_0 the free electron mass. The electron energy is related to k through the parabolic dispersion relation; $f_S(E)$ in (1) is the Fermi function for the source contact, which gives the probability that such an electron is injected from the contact; $T(E)$ is the transmission coefficient for the electron; and $f_D(E)=f_S(E+qV_{DS})$ is the Fermi function at the drain contact. Eq. (1) can be developed obtaining the following result:

$$I_B = \frac{qkT}{\pi\hbar}\sum_{v}\sum_{n} g_v \ln\left\{\frac{1+e^{\frac{E_{FS}-E_n^v(x_{max})}{kT}}}{1+e^{\frac{E_{FD}-E_n^v(x_{max})}{kT}}}\right\} \qquad (2)$$

where I_B refers to the current under the ballistic transport hypothesis. Eq. (2) can be rewritten as a simple function of the forward and backward directed fluxes as:

$$I_B = I^+ - I^- = W\ q\ (F^+ - F^-) \qquad (3)$$

Where W, F$^+$, and F$^-$ are the channel width, the incident flux from the source, and the incident flux from the drain, respectively. The potential and charge distribution of the intrinsic DG structure has been reported by Taur[6,7]. A simple one flux representation of channel transport in the nanoscale MOSFET is shown in Fig. 2. This flux formulation will be useful for introducing the scattering, as we will explain in the next section.

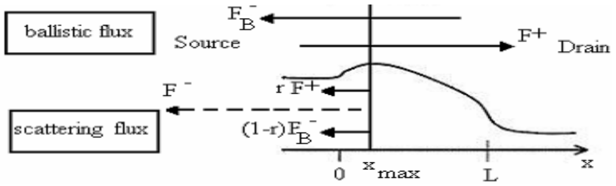

Fig. 2. Simple one flux representation of channel transport in nanoscale MOSFETs.

3. Scattering model for the current

In the presence of scattering, the negative directed flux (F^{--}) contains a component (rF^+) due to the backscattering of the positive directed flux injected from the drain and another component (1-r)F_B^- corresponding to the fraction of the flux injected from the drain (F_B^-) that transmits towards the source. This can be clearly seen in Fig. 2. By adding the source and drain related contributions, we find

$$F^- = rF^+ + (1-r)F_B^-$$

(4)

By subtracting the positive and negative directed fluxes, as in Eq. (4), the current including scattering can be calculated as:

$$\begin{aligned} I &= W\,q\,\left\{F^+ - rF^+ - (1-r)F_B^-\right\} \\ &= W\,q\,(1-r)(F^+ - F^-) = (1-r)I_B \end{aligned} \qquad (5)$$

The backscattering coefficient r is related to the critical channel length ℓ and the low field momentum relaxation length λ is given by:

$$r = \frac{\ell}{\ell + \lambda} \qquad (6)$$

In Fig. 3, the output characteristics of the DG-MOSFET on the presence of scattering are shown. The solid lines are calculated by Eq. (5), and the symbols are the numerical 2-D NEGF simulations obtained with nanoMOS. Good agreement with nanoMOS numerical simulations has been obtained.

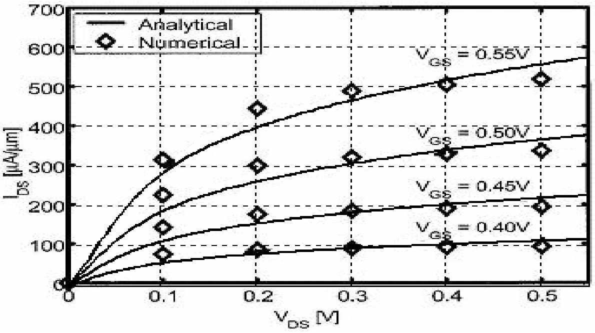

Fig. 3. Comparison of the output characteristics of the modeled DG-MOSFET. The solid line results of our compact model, and the diamonds represents 2D numerical simulation of the same device.

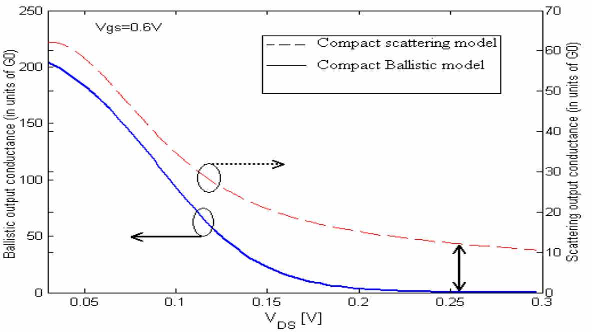

Also, the predicted channel conductance does not tend to zero (see Fig. 4), as in the ballistic case, because of the non-saturating electron velocity near the source end.

Fig. 4. Channel conductance for the DG-MOSFET. The dotted line is the result from our compact scattering model (r≠0), and the solid line from the ballistic model (r=0). G_0 is the quantum conductance unit ($=q^2/\pi\hbar$).

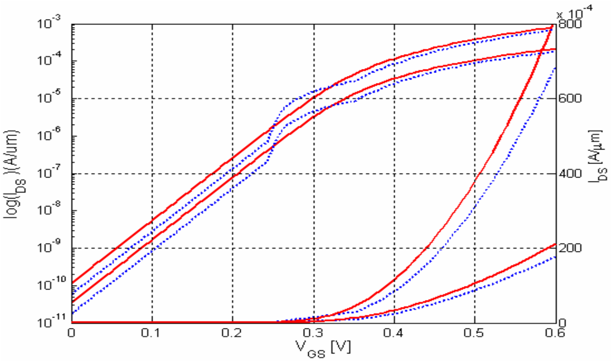

Fig. 5. Comparison of the transfer characteristics between our model (solid lines) and the model presented in[5] (dotted lines). Plots in linear and log scales for low (V_{DS}=0.05V) and higher (V_{DS}=0.55V) drain biases.

Fig. 5 introduces a comparison between the transfer characteristics (I_{DS} versus V_{GS}) obtained with our proposed model (solid lines), and with the model presented by[5] (dotted lines). The characteristics are plotted for low (V_{DS}=0.05V) and higher (V_{DS}=0.55V) drain bias conditions. We demonstrate that our model can be used to describe both subthreshold and above threshold behavior. A discontinuity was observed in the model of[5] at the transition between below and above threshold, whereas our model does not suffer from this discontinuity.

4. Conclusions

A compact DG-MOSFET which includes scattering has been introduced in this work, based on the McKelvey theory. Our model is continuous from below to above threshold and from linear to saturation regions, without suffering from discontinuities, as presented in other models. A good agreement with 2-D numerical simulations (nanoMOS) is obtained.

5. References

[1] D. Jiménez et al.., *J. Appl. Phys*., vol. 94, pp. 1061-1068, 2003.
[2] D. Jiménez et al.., *Proc. ESSDERC Conf. 2003*, pp. 187-190.
[3] M. Lundstrom, *IEEE Electron Device Lett.*, vol. 18, 1997.
[4] J. P. McKelvey et al., *Phys. Rev.*, vol. 123, pp. 51–57, 1961.
[5] A. Rahman et al., *IEEE Trans. Electron Devices*, vol. 49, 2002.
[6] Y. Taur, *IEEE Electron Devices Lett.*, vol. 21, pp. 245-247, 2000.

[7] Y. Taur, *Fundamentals of VLSI Devices*, Cambridge University Press, 1998.

Improvement of the selectivity of SnO_2 and Pt-SnO_2 thick film gas sensors via zeolite films

P. Ivanov[1], M. Vilaseca[2], E. Llobet[1], X. Vilanova[1], J. Hubalek[3], J. Coronas[2], J. Santamaría[2], X. Correig[1]

[1]Department of Electronic and Electrical Engineering, University Rovira i Virgili, Tarragona, Spain
[2]Department of Chemical and Environmental Engineering, University of Zaragoza, Zaragoza, Spain
[3]Faculty of Electrical Engineering and Communication, Brno University of Technology, Brno, Czech Republic

Abstract

Thick film pure and Pt-doped SnO_2 gas sensors covered with zeolite films (zeolite A and silicalite) were fabricated and their gas sensing properties for ethanol, ammonia, benzene and methane, were studied. The results clearly indicate that, a suitable zeolite layer could dramatically increase the selectivity of the sensors.

1. Introduction

The detection and monitoring of toxic and/or noxious gas emissions is extremely important for human and animal safety, and environmental protection. Ammonia (NH_3) emissions such as those produced by agricultural activities (e.g. livestock buildings) are a major environmental problem, particularly in the neighborhood of urban settlements. Benzene vapors (C_6H_6) represent another serious environmental problem. It has been demonstrated that the presence of benzene in the soil could be an indicator of oil reservoirs and environmental contamination [1]. The detection of these substances in atmospheric air, in water and in soils is therefore attracting intensive research efforts with in view to develop cheap and selective sensors. Although metal oxide gas sensors are inexpensive and very sensitive to different toxic gases, they still suffer from serious shortcomings such as the lack of selectivity. In this context, the use of zeolite coatings could be of help to increase their selectivity.

2. Sensor fabrication

Sensors were fabricated by thick-film technology on an alumina substrate. Figure 1 shows the layout of the sensors. To synthesize the paste a commercially available tin oxide powder was milled together with xylene in a planetary ball mill. Then, the milled powder was mixed with an organic vehicle based on therpineol. The paste, which was homogenized in a mortar, had the appropriate viscosity and rheology for screen-printing. For the doped layers, Pt particles with nanometric size were introduced in the paste before the printing. The active layer printed over the gold electrodes with a screen mesh 280/30 μm was highly homogeneous and adhered very well to the Al_2O_3 substrate. The sensors were dried (5 minutes at 100ºC and 10 minutes at 150ºC) and then fired in a furnace at 650ºC. After that, the sensors were slowly cooled to ambient temperature [2].

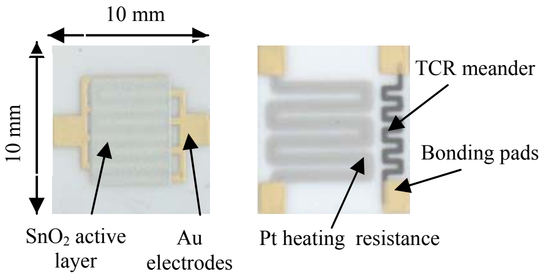

Fig. 1 Sensor design.

To increase the selectivity of the semiconductor metal oxide sensors, two different zeolite films were tested onto pure and Pt doped SnO_2 thick-film layers. Zeolite A layers (hydrophilic) were prepared on the SnO_2 active layer by seeded growth: first, active layers were covered with commercial zeolite A seed crystals (~2 μm) by rubbing, then sensors were placed vertically in Teflon lined stainless steel autoclaves and 3 consecutive hydrothermal synthesis were carried out at 80ºC for 5h with composition: $80Na_2O$: $1Al_2O_3$: $9SiO_2$: $5000H_2O$. After crystallization sensors were removed from the solution, washed with de-ionized water until neutral pH, and dried at 50ºC. Silicalite (organophilic) modified sensors were prepared by a similar procedure but in this case sensors were seeded in situ by placing them in autoclaves at 130ºC for 2 h with a mixture of the following composition: $10SiO_2$: 2.4TPAOH: 1NaOH: $110H_2O$, where TPAOH, the structure-directing agent, is tetrapropylammonium hydroxide. A second hydrothermal treatment at 175ºC for 18 h in a synthesis gel of composition: 1TPABr: 4.5TEOS: 1KOH: $1000H_2O$, where TPABr is tetrapropylammonium bromide and TEOS tetraethylorthosilicate, completes the zeolite layer synthesis. Finally, all the zeolite samples were washed with de-ionized water, dried and annealed at 480ºC for 8h to remove the structure-directing agent. The responses obtained with these sensors were compared against the responses of the same sensors without the zeolite layers. This showed that the zeolite layers changed significantly the sensitivity of the sensors.

3. Results and discussions

3.1. Structural characterization

The quantitative analysis made by Energy dispersive X-ray Spectroscopy (EDX) showed that the percentage of the Pt doping was approximately 1.5% in weight. Figure 2 shows a SEM analysis of a non-doped SnO_2 sample (a), and a zeolite A layer formed on the sensor (b).

3.2. Gas sensitivity measurements

The gas sensor performance was tested in a thermally controlled chamber. The sensors operating temperature was adjusted successively to 250ºC, 300ºC and 350ºC. We introduced the measured species (ethanol, ammonia and benzene) into the test chamber by using high precision chromatographic syringes. Dry air was used as a reference gas. The liquid quantities necessary were consecutively injected to create concentrations of 10, 100 and 1000 ppm for each of the contaminants.

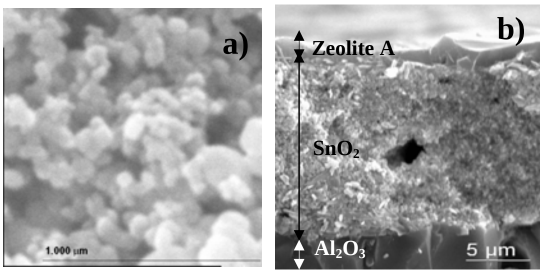

Fig. 2 SEM micrographs of a) surface of a non-doped SnO_2 thick-film sensor, b) section view of a zeolite A modified sensor.

Between every two measurements a pause of 30 minutes was made. The electrical resistance of the sensors was monitored using an HP 34970A resistance acquisition system. Figure 3 shows the typical response of the tested sensors working at 350 ºC to successive injections of ammonia.

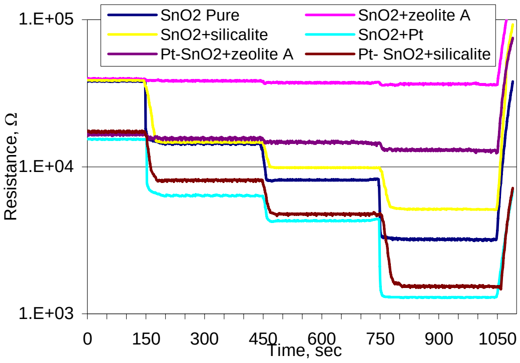

Fig.3 Typical response of the tested sensors working at 350 ºC to successive injections of ammonia.

To study the sensitivity of each sensor, we calculated ratio between the baseline resistance (i.e., in air) and the resistance in the presence of a gas species (R_a/R_g). Some of the results obtained are presented in Tables 1 to 3.

Table 1. Response to the non-modified layers

Gas/ Concent.(ppm)		*SnO_2*			*SnO_2+Pt*		
		250°C	300°C	350°C	250°C	300°C	350°C
Ethanol	**10**	5.14	7.26	3.04	20.16	78.51	9.10
	1000	19.94	62.30	38.92	120.07	524.66	19.10
NH_3	**10**	1.14	1.06	2.45	1.56	2.43	7.34
	1000	1.51	1.31	3.60	5.11	6.03	11.32
C_6H_6	**10**	1.02	1.03	1.21	1.04	1.06	1.48
	1000	1.16	1.67	2.62	2.06	2.49	4.77

Table 2. Response to the zeolite modified layers

Gas/ Concent.(ppm)		*SnO_2 + zeolite A*			*Pt-SnO_2 + zeolite A*		
		250°C	**300°C**	**350°C**	**250°C**	**300°C**	**350°C**
Ethanol	**10**	5.09	7.14	3.01	19.85	78.45	9.04
	1000	19.24	61.56	38.76	119.23	521.57	18.73
NH_3	**10**	1.01	1.01	1.02	1.11	1.24	1.34
	1000	1.04	1.06	1.07	1.26	1.30	1.50
C_6H_6	**10**	1.01	1.03	1.20	1.06	1.09	1.53
	1000	1.14	1.63	2.58	2.08	2.52	4.79

Table 3. Response to the silicate modified layers

Gas/ Concent.(ppm)		*SnO_2 + silicate*			*Pt-SnO_2 + silicate*		
		250°C	**300°C**	**350°C**	**250°C**	**300°C**	**350°C**
Ethanol	**10**	1.25	1.82	1.38	1.23	4.06	1.05
	1000	4.37	8.75	6.23	10.40	17.10	2.40
NH_3	**10**	1.12	1.05	2.41	1.53	2.37	7.14
	1000	1.49	1.29	3.55	5.01	5.83	10.88
C_6H_6	**10**	no	no	no	1.00	1.02	1.04
	1000	no	no	no	1.12	1.21	1.22

In general, for all of the species tested, the Pt doped layers showed higher sensitivity. From the data presented in table 2 we can conclude that the layers modified by zeolite A show a lower response to NH_3, keeping unchanged their response to benzene and the ethanol. On the other hand, the silicalite-modified layers (Table 3) reduce dramatically their response to ethanol and benzene, keeping unchanged their response to ammonia.

4. Conclusions

In this paper we have described the fabrication of pure and Pt-doped thick-film SnO_2 gas sensors modified with zeolite A and silicalite layers. Their response to ethanol, ammonia and benzene was studied. The obtained results clearly show the potential of zeolite-based sensors to achieve a higher selectivity/sensitivity for gas sensing applications. Gas sensitivity tests are in progress to determine the sensor response to NO_2, CO and humidity.

References

[1] J. Getino, L. Ares, J. I. Robla, M. C. Horrillo, I. Sayago, M. Fernandez, J. Rodrigo, J. Gutierrez, *Sens. Actuators B* 59 (1999), pp. 249-254.

[2] P. Ivanov, E. Llobet, X. Vilanova, J. Brezmes, J. Hubalek and X. Correig, *Sens. Actuators B*, In Press

Modeling of Kerr Nonlinear Photonic Crystal Slabs with the FDTD method

I. S. Maksymov, L. F. Marsal* and J. Pallarès

Departament d'Enginyeria Electrònica, Elèctrica i Automàtica, Universitat Rovira i Virgili, Campus Sescelades, Avda. Països Catalans 26, 43007 Tarragona, Spain. E-mail: lmarsal@etse.urv.es

Abstract.

The finite-difference time-domain method is used for analyzing band structures in two-dimensional Kerr-nonlinear photonic crystal slabs. Results show red-shifting of the band structure due to the nonlinearity and the incident intensity.

1. Introduction

At present, the study of nonlinear photonic crystals is of particular interest because of promising applications in photonic devices [1]. Both one- and two-dimensional infinite Kerr-nonlinear photonic crystals have been studied numerically in [2-5]. However, in contrast to infinite structures, finite ones are feasible and would provide some specific properties due to the confinement in the vertical direction.

2. Numerical method

Let us consider the Maxwell equations

$$\nabla \times \mathbf{E} = -\frac{\partial \mathbf{H}}{\partial t}, \quad \nabla \times \mathbf{H} = \frac{\partial \mathbf{D}}{\partial t}, \qquad (1)$$

where $\mathbf{E}$ and $\mathbf{H}$ are electric and magnetic fields; $\mathbf{D}$ is the electric displacement. In order to solve equations (1), we need so-called constitutive equation that relates $\mathbf{D}$ to $\mathbf{E}$. For the Kerr-nonlinear medium, the dielectric constant depends on the electric field The constitutive equation is written as

$$\mathbf{D} = \varepsilon_0 \left(\varepsilon' + \chi^{(3)} |\mathbf{E}|^2 \right) \mathbf{E}, \qquad (2)$$

where ε' is intensity-independent dielectric constant.
In accordance with the Bloch theorem for a periodic structure, we can impose the periodic boundary conditions (BC) for the fields $\mathbf{E}$ and $\mathbf{H}$. In order to take into account the air region above and below the slab (i.e., the confinement in the vertical direction), we set the Mur absorbing boundary conditions (ABC) [6] of the second order at $z = \pm 1.5a$.

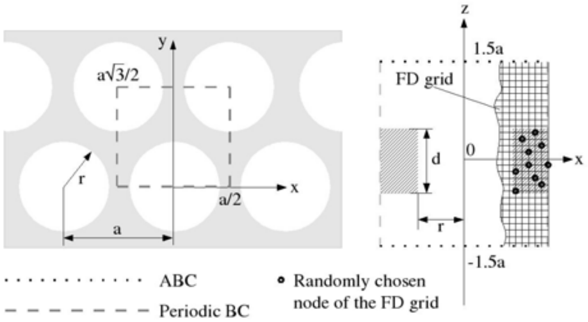

Fig. 1. The computational domain in the real space for the calculation of the band structure and the BC used to truncate it: (left) top view, (right) side section view. A part of the finite-difference (FD) grid is shown. The Dirac delta function excites the structure in randomly chosen nodes of the FD grid.

The incident intensity is simulated with the Dirac delta pulse with the amplitude I_{inc}. At the first step of the calculation process, only those randomly chosen nodes of the finite-difference (FD) grid that are situated within the slab are excited, while all field components in other nodes are set to be zero (see Fig. 1).

3. Results and discussion

We consider a triangular lattice of circular air rods ($a = 1$, $r = 0.24a$) in a Kerr-nonlinear material ($\varepsilon' = 12$, $\chi^{(3)} = 0.01$). The PC slab is suspended in air, its thickness is $d = 0.3a$. The computational domain in the real space for the calculation of the band structure and the BC used to truncate it are shown in Fig. 1. In the z-direction, the computational domain is divided onto 70 cells. In the directions of the periodicity, it is divided onto 200 cells. The total number of the time steps is about $2^{14} \div 2^{15}$.
The calculated band structures (TE-like modes) are shown in figures 2 (a) and 2 (b) for the incident intensities I_{inc} = 3000 and I_{inc} = 10000 arbitrary units (a.u.), respectively. They are compared with the band structure in the linear 2-D PC slab ($\chi^{(3)} = 0$, $I_{inc} = 1$ a.u.). The shaded region denotes the light cone.

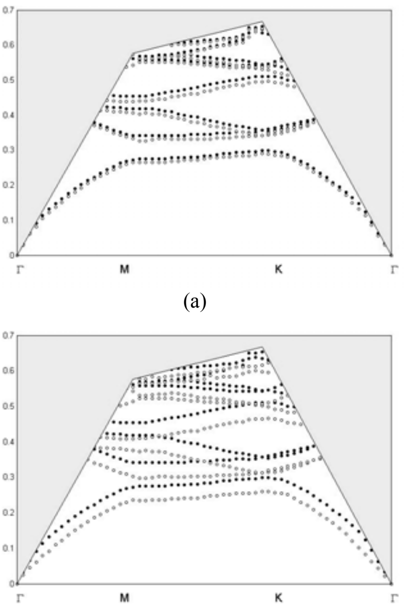

(a)

(b)

Fig. 2. Band structures (TE-like modes) in the linear (solid circle) and Kerr-nonlinear (open circle) 2-D PC slabs. In the nonlinear case, the incident intensities are $I_{inc} = 3000$ a.u. and $I_{inc} = 10000$ a.u. The shaded region denotes the light cone.

It can be seen that the bands of the band structures in the nonlinear slab are red-shifted with regard to the linear case and that the red-shift increases as the incident intensity increases. From the analysis of the changes in the dielectric constant [7], it can be deduced that $I_{inc} = 1$ a.u. corresponds to an intensity of about $0.5\ W / cm^2$. The dynamical change of the band structure is the basis for intensity-driven optical limiting and all-optical switching [5].

In Fig. 3, we present the calculated gap map (TE-like modes) in the Kerr-nonlinear 2-D PC slab shown in figure 1. The shaded region represents the linear case. The dashed and solid lines represent the nonlinear case at the incident intensities $I_{inc} = 3000$ a.u. and $I_{inc} = 10000$ a.u., respectively. There are no band gaps in the TM-like modes for any hole radius and intensity. Therefore, there are no complete band gaps.

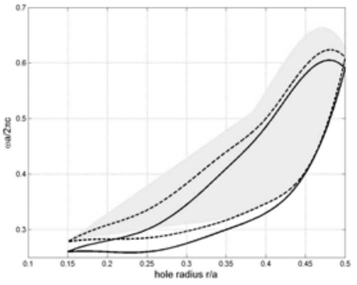

Fig. 3. Calculated gap map (TE-like modes) in the linear and Kerr-nonlinear 2-D PC slabs. The shaded region represents the linear case. The dashed and solid lines represent the nonlinear case at the incident intensities $I_{inc} = 3000$ a.u. and $I_{inc} = 10000$ a.u.

As can be seen from figure 3, the red-shift of the band gap is maximal when the air rod radius is in the range $0.2a$ to $0.25a$. It can be explained by the fact that the portion of the nonlinear material decreases as the radius of the air holes increases. As the result, it leads to the decrease in the red-shifting. On the other hand, the portion of the nonlinear material increases as the radius of the air holes decreases. Such a decrease in the radius gives rise to evanescing band gaps.

4. Conclusions

An FDTD analysis of band structures in Kerr-nonlinear 2-D photonic crystal slab has been presented. The results have shown that the band structures in the Kerr-nonlinear 2-D photonic crystal slab are red-shifted with regard to the linear case. The red-shift has been explained in terms of the increasing in the dielectric constant of the slab. The red-shift of the gap between the first and the second bands increases as the incident intensity increases. The maximal increase has been achieved when the air rod radius is in the range $0.2a$ to $0.25a$.

Acknowledgments

This work was supported by the Spanish Commission of Science and Technology (CiCYT), project No. TIC2002-04184-C02

References

[1] R. E. Slusher and B. J. Eggleton. *Nonlinear Photonic Crystals*, Springer Verlag, Berlin, 2003.
[2] P. Tran, *Phys. Rev. B* **52**, 10673, 1995.
[3] V. Lousse and J. P. Vigneron, *Phys. Rev. E* **63**, 027602, 2001.
[4] A. Huttunen and P. Törmä. *J. Appl. Phys.* **91**, 3988, 2002.
[5] I. S. Maksymov, L. F. Marsal and J. Pallares. *Opt. Commun.* **237**, 378, 2004.
[6] A. Taflove, *Computational Electrodynamics*, Artech House, Boston, 1995.
[7] C. Lixue, D. Xiaoxu, D. Weiqiang, C. Liangcai and L. Shutian, *Opt. Commun.* **209**, 491, 2002.
[8] I. S. Maksymov, L. F. Marsal and J. Pallares. *Proc. of the 12th Int. Workshop on Optical Waveguide Theory and Numerical Modelling*, Ghent, Belgium, 2004.

Diode-like conduction in broken down MOS devices

Enrique Miranda

Departament d'Enginyeria Electrònica, Universitat Autònoma de Barcelona, 08193 Bellaterra, Spain
Tel.:93-581-3138, e-mail: enrique.miranda@uab.es

Abstract

The post-breakdown current in MOS devices with ultra-thin SiO_2 oxides (t_{ox}< 5 nm) is investigated within the framework of a diode-like conduction model with high series resistance. The diode-like behavior is ascribed to the contact effect between the semiconductor electrodes and the series resistance is mainly attributed to the crowding of the current lines at the nanometer-sized constriction which represents the breakdown path. It is shown how this model is able to capture some distinctive features exhibited by the normalised differential conductance and how the model parameters can be extracted from the experimental characteristics.

1. Introduction

More than a decade ago, Nafría *et al* [1], pointed out that the post-breakdown current-voltage (I-V) characteristic of a MOS structure with an ultra-thin oxide could be explained in terms of a diode with a series resistance. Even though they did not provide at that time any analytic expression for the current, they put in evidence three distinctive features of post-breakdown conduction: *i)* the rectifying character of the leakage path, i.e. the large asymmetry between forward and reverse currents, *ii)* the exponential dependence of the forward characteristic at low voltages (< 1 V), and *iii)* the resistive behavior at larger bias. These experimental observations were supported and extended by a number of subsequent papers [2,3]. Understanding the conduction mechanism in SiO_2 after the occurrence of a breakdown event is important not only because it can provide us clues about the causes that lead to such event but also because it is a necessary step towards the development of suitable simulation tools for MOSFETs devices operating under this circumstance [4].

2. Model and experimental results

The proposed approach consists in representing the breakdown path by a diode with a series resistance R, as schematically illustrated in Figs. 1a and 1b. The resulting I-V characteristic can be written as:

$$I(V) = I_0\left\{\exp\left[\alpha\left(V - IR\right)\right] - 1\right\} \tag{1}$$

where I_0 and α are constants. Notice that Eq.(1) is an implicit equation since the current appears simultaneously in both terms. Eq.(1) can be solved using the Lambert-W function [5], but this formulation is cumbersome and unnecessary in what concerns with the parameter extraction process.

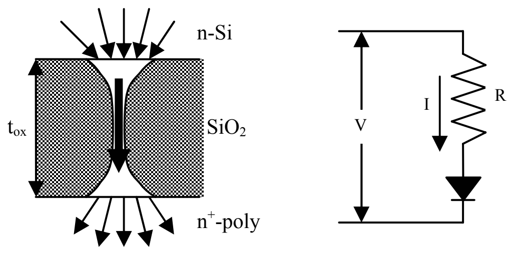

a) b)

Fig. 1- a) Schematic representation of the breakdown path across the oxide layer. b) Equivalent circuit for the breakdown path formed by a diode and a series resistance R.

In the case of Schottky diodes, I_0 is called the saturation current and α is the inverse of the thermal voltage kT/e, where k is the Boltzmann's constant, T the temperature and e the electron charge. It is a common practice to introduce a correction factor n called the ideality factor which multiplies the thermal voltage, namely $\alpha=e/nkT$. While for ideal contacts n is close to the unity, it has been found that a number of systems such as metal-semiconductor nanocontacts [6] MIS Schottky barriers [7], porous silicon diodes [8] and p-n junctions [9] exhibits larger factors ($n\geq5$). As we will show below, this is precisely our case so that, following Ref.[6], we prefer to refer to α instead of the terminology used for macroscopic diodes. As evidenced by the vast number of experimental works, Eq.(1) seems to represent a wide variety of rectifying contacts independent of their particular features. Nevertheless, it should be pointed out that ideality factors between 1 and 2 have been previously reported for hard breakdown conduction as well [1,2].

The samples used in this work are standard MOS capacitors with oxides 2.1, 3.0, 3.8, 4.3, and 4.9 nm thick, n-type substrates (10^{15} cm^{-3}), and n^+-polysilicon gates with areas of 10^{-4} cm^2. Figure 2 shows a typical post-breakdown I-V characteristic in linear axes for a sample with a 4.3 nm thick oxide. As previously mentioned, the current increases exponentially below approximately 1 V becoming seemingly linear for higher voltages. However, when the normalised differential conductance g=d(lnI)/d(lnV) is plotted (see

Fig. 2), the detailed behavior of the characteristic is revealed. The shape of the curve can be understood analyzing the limiting cases of Eq.(1):

$$g = \frac{d(\ln I)}{d(\ln V)} \approx \begin{cases} \alpha V & V << 1 \\ 1 & V >> 1 \end{cases} \qquad (2)$$

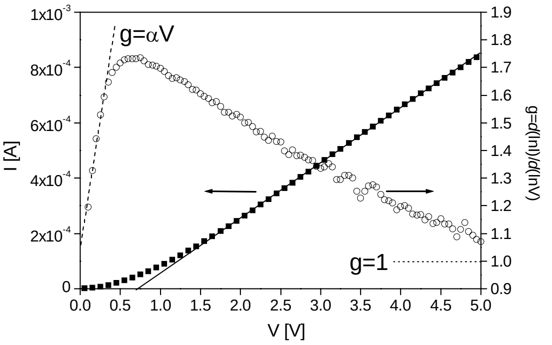

Fig. 2- Experimental I-V (filled squares) and g-V (hollow circles) post-breakdown characteristics for a 4.3 nm thick sample. The solid line is a guide to the eye emphasising the seemingly linear behavior of the current. The dashed and dotted lines show the limiting cases of Eq.(1).

3. Extraction of model parameters

A number of different procedures have been proposed to extract the parameters of Eq.(1) from the experimental data [10]. However, due to nowadays computing facilities we can proceed in a direct way. We interchange the voltage and current axes as illustrated in Fig. 3. Mathematically, this corresponds to the equation:

$$V = RI + \frac{1}{\alpha} \ln\left(\frac{I + I_0}{I_0}\right) \qquad (3)$$

Next, the parameters are found using a nonlinear least-squares algorithm. In Fig. 3, experimental and fitting results for a set of characteristics measured on different devices are shown. Firstly, α ranges between 3.7 and 8.7 V^{-1} so that the equivalent ideality factor would run from 4.4 to 10.4 at T=293 K. We cannot offer an explanation for such values but in other systems large ideality factors have been attributed to the sum of individual rectifying junctions, surface states, the presence of an interface oxide layer and electron-hole recombination currents. Secondly, the series resistances are found in the range from 1.8 kΩ to 5.7 kΩ, which is, disregarding the contribution of the substrate resistance, in agreement with the theoretical result R=5.5 kΩ reported in Ref. [11]. In this latter work, the breakdown path was simulated assuming a cylinder shape n^+-polysilicon conductor between gate and substrate with a radius of 5 nm. This result strongly supports the idea that the breakdown path connecting the semiconductor electrodes behaves as a nanometre-sized rectifying point contact.

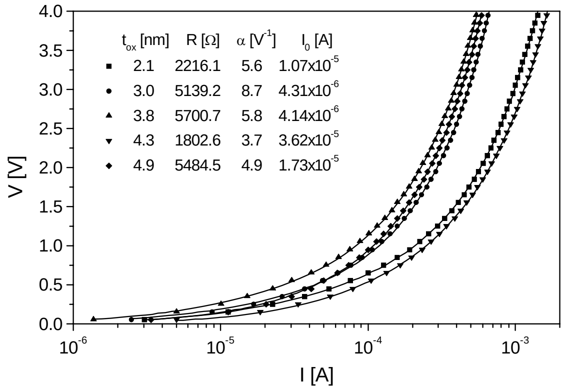

Fig. 3- Experimental V-I characteristics for a set of samples with different oxide thicknesses (symbols) and fitting results (solid lines) using Eq.(1).

4. Conclusions

In summary, we have shown that the post-breakdown I-V characteristic of a MOS structure can be modelled as a diode with series resistance. Within this framework, the differential normalised conductance has proved to be a powerful tool for analyzing the current behavior in detail. A simple method to extract the model parameters based on exchanging the current and voltage axes and the direct fitting of the experimental data was discussed. We believe that this new approach to the conduction problem is a step forward toward a deeper understanding of the post-breakdown electron transport mechanism in ultra-thin dielectric layers.

Acknowledgements

The author acknowledges the support of the Ministerio de Ciencia y Tecnología (Spain) under project number TIC2003-08213-C02.

References

[1] M. Nafría *et al*, J. Appl. Phys. 73, 205 (1993).
[2] A. Halimaoui *et al*, Microelec. Eng. 36, 157 (1997).
[3] K. Umeda *et al*, J. Appl. Phys. 82, 297 (1997).
[4] B. Kaczer *et al*, IEEE Trans. Electron. Dev. 49, 507 (2002).
[5] A. Ortiz-Conde *et al*, Solid-St. Electron. 44, 1861 (2000).
[6] J. Marchand *et al*, J. Appl. Phys. 54, 7034 (1983).
[7] W. Kang *et al*, J. App. Phys. 78, 1101 (1995).
[8] K. Molnár *et al*, Phys. Stat. Sol. (a) 197, 446 (2003).
[9] J. Shah *et al*, J. Appl. Phys. 94, 2627 (2003).
[10] V. Aubry *et al*, J. Appl. Phys. 76, 7973 (1994).
[11] T. Hosoi *et al*, in *Proc.* IEEE IEDM, USA, 2002, p. 121.

Fabrication and Characterization of thick oxidized porous silicon in RF

D. Molinero[1], E. Valera[1], A. Lázaro[2], A. Rodriguez[1], L. Pradell[2], R. Alcubilla[1]

[1] Departament d'Enginyeria Electrònica, Universitat Politècnica de Catalunya, C/ Jordi Girona 1-3, mòdul C4, Campus Nord, 08034 Barcelona, Spain

[2] Departament de Teoria de Senyal i Comunicacions, Universitat Politècnica de Catalunya, C/ Jordi Girona 1-3, mòdul D3, Campus Nord, 08074 Barcelona, Spain

Abstract

This work focus on the electromagnetic properties of oxidized microporous silicon films exploring their use as insulators in RF applications. Porous silicon layers have been fabricated by anodic reaction and oxidation, In order to characterize these films at RF frequencies, simple transmission lines have been fabricated. Material parameters are deduced from scattering measurements

Keywords.- Coplanar waveguide (CPW), Oxidized porous silicon (OPS), thick dielectric film.

1. Introduction

In the microwave region, high-resistivity silicon substrates are widely used because of its low dielectric losses. Unfortunately, high resistivity Silicon is not appropriate for integration with silicon active devices. If low resistivity silicon has to be used, thick dielectrics layers acting as isolation materials should be included [1]. Among those insulating layers, oxidized porous silicon layers avoid the dielectric losses introduced by a low resistivity substrate while keeping low cost and short fabrication time, comparing favourably with Chemical Vapour Deposited dielectrics.

2. Fabrication Process

Oxidized porous silicon layers (OPSL) were obtained by anodization and oxidation of silicon substrates. A special Teflon set-up was used for the anodization process. The detailed fabrication sequence of the OPSL is schematized in Figure 1. The starting material was 1-10 Ω.cm resistivity <100> p-type boron doped silicon wafers. In the backside of the wafer a thin film of aluminum was deposited (Fig. 1a). PS layers were obtained by electrochemical etching (ECE) in hydrofluoric acid (HF) and ethanol (C_2H_5OH) electrolyte solution ($HF_{50\%}$:C_2H_5OH = 1:1) (Fig. 1b). During the process current density was kept constant. PSL films in this work were fabricated at room temperature, with 10mA/cm^2 anodization current. Growth rate of 0.5µm/min was measured by SEM. The aluminum was etched away after anodic reaction process (Fig. 1c). PSL is preoxidized at 500ºC under atmospheric pressure dry oxygen for 30 min. to avoid coarsening of porous silicon. Then, a new oxidation at 900ºC was needed under atmospheric pressure wet oxygen for several minutes to form OPS layers (Fig. 1d). The test circuits consist of transmission lines. To take advantage of field localization at the surface of the substrate and weak substrate height dependence, finite ground coplanar waveguide transmission lines (FGCPW) are used (see Fig.1 for a cross-section). The CPW lines consist of two consecutive layers of sputtered Ti / Au (Fig. 1e). To form the metal pattern, the metal on the OPSL was etched using a metal etchant (Fig. 1f). Au was etched out easily but the etching of titanium layer needed much caution because buffer HF used to Ti etching solution also etches the SiO2 layer. A 1 Ωm thick sputtered gold layer is used in all the samples. In order to compare microwave performance several samples are investigated. The main parameters are shown in table 1.

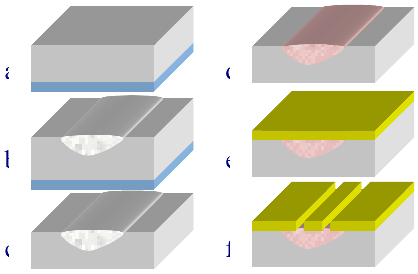

Fig. 1: Fabrication sequence of the oxidized porous silicon layers (OPSL).

3. Results

All circuits were measured up to 26 GHz using 8510C network analyzer using Cascade on-wafer probe station. The LRRM (Load-Reflect-Reflect-Match) method is used for on-wafer S-parameter calibration. From the Scattering parameter measured data, the chain ABCD parameters of the lines can be obtained successfully, and then, the characteristic impedance (Z_0), effective dielectric constant (ε_{ref}) and attenuation constant (γ) are calculated. From the effective dielectric constant an estimation of the porosity P can be obtained. Effective dielectric constant ε_{ref} is a function of CPW aspect ratio (W/(W+2S) and can be computed using two-dimensional simulation (Agilent Momentum). The observed variation in ε_{ref} is less than 5% for large aspect ratio variation. Also the effective dielectric constant can be approximated as:

$$\varepsilon_{ref} \approx \frac{\varepsilon_r + 1}{2} \qquad (1)$$

The relative dielectric constant can be estimated using this model:

$$\varepsilon_r = \frac{(H_S + H_P)\cdot\varepsilon_{r,Si}\cdot\varepsilon_{r,OPS}}{\varepsilon_{r,Si}\cdot H_P + \varepsilon_{r,OPS}\cdot H_S} \qquad (2)$$

A simple volumetric approximation can be used to predict the relative dielectric constant of the porous material as:

$$\varepsilon_{r,OPS} = \varepsilon_{r,Si}\cdot(1-P) + \varepsilon_{r,Air}\cdot P \qquad (3)$$

Figure 2 shows the extracted effective dielectric constant at 10 GHz for 15 µm and 10 µm oxidized porous silicon using three oxidation methods. The extracted porosity from the measured effective dielectric constant using (3) is listed also in table 1. This table shows the measured attenuation. These results show that low temperature oxidation produces less attenuation due the fewer apparitions of the silicon columns. Figures 3-5 compare the microwave performances (up to 26 GHz) of oxidized porous silicon layers polyimide (ε_r=2.9) buffer layers (with 10 µm and 20 µm thickness) and a combination of 10 µm thickness of polyimide over a 10 µm OPS thickness layer. All the samples uses the same low resistivity silicon substrate (270 µm, 20 Ω·cm) and metal lines of 1 µm of gold. For closed characteristic value lines with thick polyimide buffer layer have better performances than OPS lines. Important improvement in attenuation is obtained when a 10 µm OPS layer with 10 µm polyimide layer is used. Also for this case the frequency dependence of characteristic impedance is reduced.

Layer Thickness	900ºC 30 min	900ºC 60 min	1100ºC 60 min
10 µm	P=84.8% α=26 dB/cm	P=82.4% α=26.5dB/cm	P=88.6% α=29 dB/cm
15 µm	P=91.1% α=25.8dB/cm	P=88.5% α=25dB/cm	P=94% α=29dB/cm

Table 1. Porosity and attenuation at 10 GHz extracted

4. Conclusions

Low resistivity silicon exhibits attenuation a factor of 20 times greater than that of high resistivity silicon. The use of oxidized porous silicon and polyimide layers reduces the total attenuation at microwave frequency band. Oxidized porous silicon offers good attenuation characteristic with low ε_{ref} on low resistivity silicon wafer using a process CMOS compatible and offers new possibilities for integrated inductors into CMOS circuits.

Acknowledgement

This work has been supported by Spanish Government Projects ref. TIC2000-0144-P4-02 and ESP2002-04141-C03-02 (MCYT)

References

[1] G. Ponchak, A Margomenos, L, Katehi “Low-loss CPW on low-Resistivity Si Substrates with Micromachined Polyimide Interface Layer for RFIC Interconnects”, IEEE- MTT vol 49 No 5, May 2001.

[2] R.L.Peterson and R.F.Drayton, "Dilectric properties of oxidized porous silicon in a low resistivity substrate", IEEE MTT-S Digest, 2001, pp.767-770

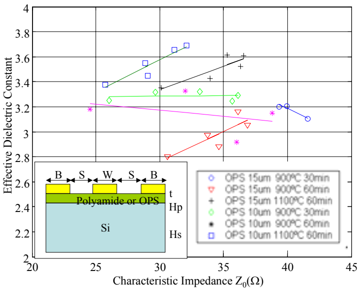

Fig. 2. Effective dielectric constant as function of Characteristic Impedance and OPS samples

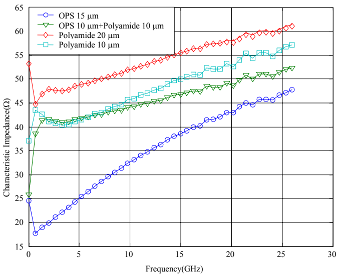

Fig. 3. Comparison between OPS and polyamide layers (Characteristic impedance)

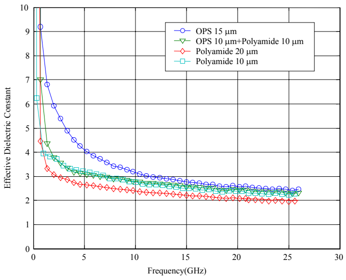

Fig. 4. Comparison between OPS and polyimide layers (Effective dielectric constant)

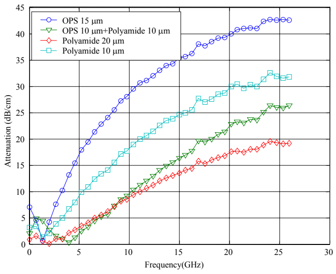

Fig. 5. Comparison between OPS and polyimide layers (Attenuation)

Er^{3+} Photoluminescence in Different Silicates Host Matrices

P. Pellegrino[1], B. Garrido[1], C. Garcia[1], M. Perálbarez[1], Y. Lebour[1], J.R. Morante[1], P. Bettotti[2], L. Pavesi[2] and M. Prassas[3]

[1]Dep. d'Electrònica, Universitat de Barcelona, Martí i Franquès 1, 08028 Barcelona, Spain
[2]Physics Department, University of Trento, Via Sommarive 14, I-38050 Povo (Trento), Italy
[3]Corning S.A., Fontainebleau Research Centre, 7bis avenue de Vilvins B.P. No.3, Avon, France

Recent spectacular advances towards the realization of a silicon-based photonic technology have come from the investigations of composite erbium/silicon systems in SiO_2 oxides. The enhancement of the erbium emission at 1.54 μm by co-doping silica with Si nanoparticles has been largely explored; leading to the demonstration of optical gain in waveguide structures where erbium-doped silicon-rich SiO_2 constitutes the active media. The main advantages of such an active media are: i) the increase in more than three orders of magnitude of the effective excitation cross section of Er; ii) the possibility to excite the Si nanoparticles in the visible with a non-coherent source and that energy is transferred very fast to a nearby Er; iii) the fact that the excitation can be performed from above or sideways instead of coaxially, simplifying and making cheaper the design of the optical pumping scheme. Furthermore, it has been demonstrated recently the possibility to excite electrically such a system, opening the way to an electrically driven optical amplifier or laser. The use of other complex silicate glasses as a host is possible and desirable. The advantages rely on the increased solubility of Er and the larger width of the Er emission in these glasses which translates into a larger optical band-width for the optical amplifier and thus the possibility to multiplex more channels in the infrared window around 1.54μm. Although some reports exist in literature about devising the composition of the active material by mixing with other compound silicate glasses, none of them explore with detail the emission behaviour as a function of the Er and Si nanoparticle concentration.

In this contribution we explore the photoluminescence properties of different silicate glasses co-implanted with silicon and Er ions to various doses. As starting materials we used soda-lime and aluminium silicates. A Si multi-implantation scheme has been adopted, in order to provide a uniform Si excess background to the subsequently implanted Er atoms. By isochronal annealing experiments the best conditions have been investigated in order to precipitate the excess implanted Si and activate the Er atoms. Optimal annealing temperatures have been found around 500 ºC, depending on the particular composition of the original glass substrate. The structural analysis of the resulting structures ensures that the best emission properties are the ones for which a phase separation between the implanted Si and the matrix occurs, even without the formation of crystalline aggregates.

A comprehensive study of the emission properties around the 1540 nm window from the processed layers has been performed as a function of the matrix characteristics, the Si and Er content in the implanted layers and the excitation wavelength and power density. As an illustrative example, in Fig. 1 we show the emission spectra of the three different matrices with the same Er content and with the amount of Si excess as a parameter. The use of the lower pump at 325 nm (non-resonant line) ensures that Er atoms are excited only through the interaction with silicon clusters, as underlined by the negligible response of the samples implanted only with Er ions (no Si excess).

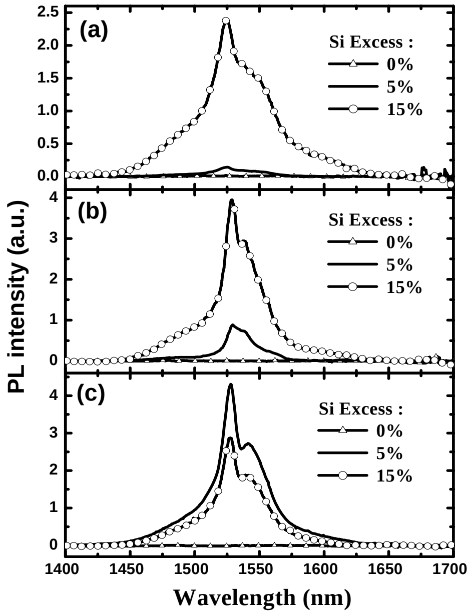

Fig. 1. PL spectra from co-implanted glass wafers excited with non-resonant line at 325 nm: (a) soda-lime (b) Al-silicate (c) fused silica.

By means of PL-rise and decay measurements both for resonant and non resonant Er-excitation, we have estimated lifetimes, in the range of 2-2.5 ms.

A systematic increase of the emission enhancement from the Er atoms due to the presence of Si cluster has been observed when increasing the excitation power (*cf.* Fig. 2). The absence of saturation of the PL curves shown in Fig. 2 demonstrates the weak absorbance of the ensemble of the Si nanoparticles coupled to Er, even if it is of course much more efficient than pumping the Er directly. In any cases the efficiency of the hybrid system is comparable for all the three matrices, as illustrated in Fig. 1.

A modelization of the interaction between the absorbing Si nanoprecipitates and the emitting Er atoms has been carried out, in order to estimate the relevant physical parameters which describe the PL process.

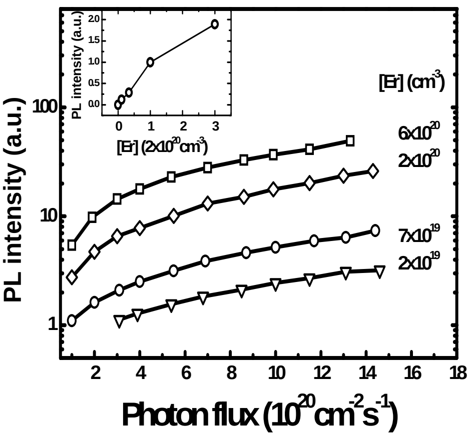

Fig. 2. PL emission at 1.54 μm as a function of the incident photon flux at 365 nm for soda-lime glasses with 15% Si excess and different Er concentrations.

Energy-filtered transmission electron microscopy (EFTEM) has revealed in pure silica and Al-silicates the presence of Si clusters with an average size of 2.5 nm, whereas none of these have been observed in soda-lime wafers treated in the same way.

The observed differences in optical behaviour of multicompound glasses respect to silica can be attributed to the more complex chemical environment around the active Er, and to the different Si clusterization occurring at the low thermal budget attainable for this kind of matrices. Low Si excess is the optimum for pure silica while high silicon excess is better for multicomponent glasses. While only Si amorphous precipitates are necessary for energy transfer in soda-lime and pure silica, it seems that even without detectable precipitation, the unique presence of a Si excess in the matrix is capable of performing a significative sensitizing action.

Thick Film Graphite Pastes for Working Electrodes of Amperometric Sensors

Jan PRÁŠEK[1], Martin ADÁMEK[1], Edgar SOTTER[2]

1. Dept. of Microelectronics, Technical University of Brno, Údolní 53, 602 00 BRNO, Czech Republic.
Tel.: +420 541 146 136, Fax: +420 541 146 298, E-mail: prasek@feec.vutbr.cz
2. Dept. Enginyeria Electrònica Elèctrica i Automàtica, Universitat Rovira i Virgili, Avd. Països Catalan, 26, 43007 Tarragona, Spain.

Abstract

This paper covers an area of thick film amperometric sensors for heavy metals detection in bulk of solution. For this reason we designed new sensor with consideration to its geometrical arrangement. In this paper there are mentioned the first results with graphite as an ecological material of working electrode that we prepared for this purpose. Finally, this working electrode is compared with classical graphite electrode arrangement.

1. Introduction

The monitoring of living environment is one of the most discussed problems in these days. One of the monitored groups of species, which is dangerous for health, is a group of heavy metals. Heavy metals are usually monitored with use of toxic mercury electrodes. One of the possibilities for ecological measurement of heavy metals is use of sensors (solid electrodes) that could be made using thick film technology (TFT) [1]. The advantage of TFT sensors are low dimensions, good reproducibility, chemical, mechanical and electrical properties of electrodes and well accessible and ecological fabrication process. The crucial advantage is low cost of electrodes (e.g. platinum electrode containing 1 mg of Pt) that enable to use of electrodes for few numbers of analyses only and big variability of used materials that do not use classical metals only (Pt, Au, Ag) but it is possible to prepare semi conductive materials, magnetic electrodes and finally it is possible to ensure reproducible nanostructure of electrodes.

The aim of this work is to prepare new type of TFT amperometric sensor with suitable working and reference electrodes with respect to ensure the best and reproducible detection limit to heavy metals contained in solutions.

2. New sensor design

Our task was to prepare new amperometric sensor substrate that will be allowed to be used for new electrode materials testing. The main emphasis was on material flexibility and reliability. Therefore we designed a new amperometric sensor substrate (fig. 1) by improving a shape of the commercial biosensor substrate [2] to our conditions. The electrodes were designed with the round shape to ensure the same electrochemical conditions in all direction of the sensor active area.

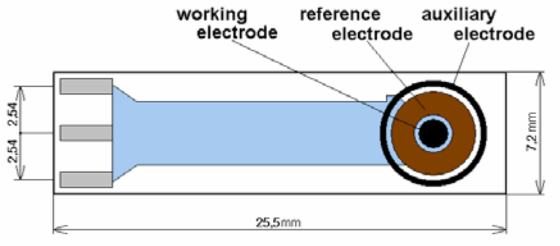

Fig.1. New sensor design.

The material of the sensors substrate is Al_2O_3. We used TFT paste ESL ESL 9562 as a material for conductive layer, ESL 9312-D for reference and auxiliary electrode and finally ESL 4913-G for the covering layer. All pastes were printed and fired using a standard TFT fabrication process recommended by manufacturer.

3. Working electrode material

The working electrode material and its surface ensure the sensitivity to dissolved species of heavy metals in solutions. Therefore the selection and preparation of working electrode material is the most important step. The graphite was chosen as the working electrode material. It is ecological and has a good sensitivity to heavy metals [3].

We prepared a few TFT working electrode materials based on graphite. This material was deposited on the sensor substrate using screen printing and dried for 15 min at 125 °C. Then, some of the pastes were fired at 520 °C. Sensor with deposited graphite working electrode is showed in the figure 2.

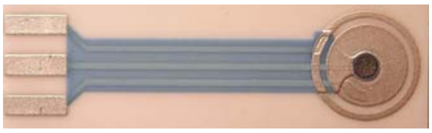

Fig.2. Base substrate with deposited graphite working electrode

4. Reference electrode preparation

The reference electrodes of all sensors were electrochemically changed into Ag/AgCl reference electrode (fig. 3) using voltammetric technique in 0,2 mol/l KCl solution mentioned in [4].

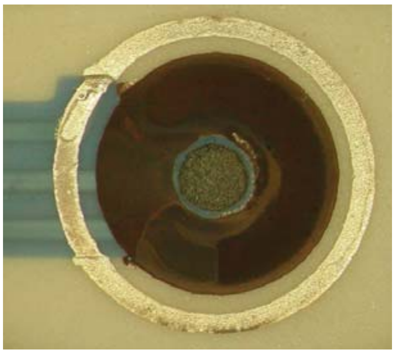

Fig.3. Detail of new sensor electrodes area with deposited AgCl layer on reference electrode.

4. Measurement

All measurements were done using two electrode system (reference and auxiliary electrode were short-circuited) in 1 mol/l KCl buffer solution with additions of 20µl 0,01 mol/l Cd^{+2} bubbled with pure N_2. The measurement method was differential pulse voltammetry in potential range -100 to -1100 mV.

5. Results and discussion

First measurements were done with use of TFT paste type C1. An example of response is showed in figure 4.

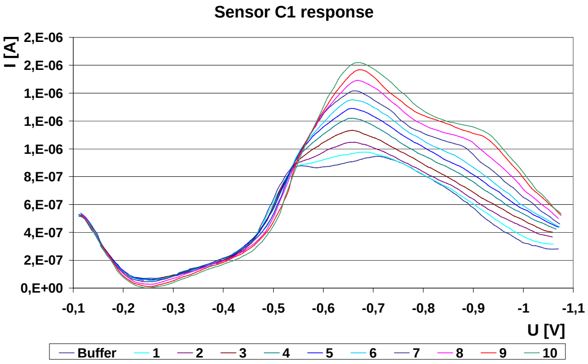

Fig.4. Response example of the sensor with deposited TFT working electrode paste type C1.

From these results was plotted the calibration curve which also contains the classical graphite electrode arrangement (graphite with paraffin wax vehicle + classical Ag/AgCl reference electrode) response for comparison (fig. 5).

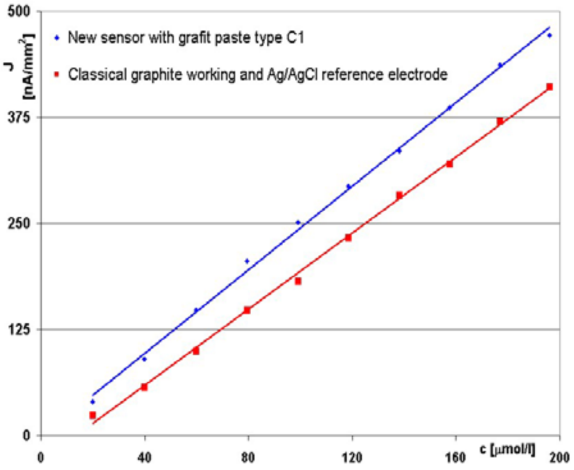

Fig.5. The comparison of calibration curves of new sensor (type C1) and classical graphite electrode arrangement.

From the calibration curve, it is obvious that the sensor could be used for heavy metals measurement. It should be noticed that the sensor with 1,5 mm^2 of working electrode active area has similar detection limit as the classical graphite electrode with working electrode area of 4,9 mm2.

6. Conclusions

From the achieved results can be said that the graphite material can be used for heavy metal detection. The achieved detection limit is 2.10^{-5} mol/l and the response is better then with use of classical graphite electrode arrangement. Other types of graphite pastes will be measured during next experiments. We assume that better detection limits will be obtained with some other types of graphite pastes that we prepared.

Acknowledgement

The work was partially supported by Czech Ministry of Education in the frame of Research Plan MSM 262200022 MIKROSYT Microelectronic Systems.

References

[1] M. Adámek, J. Prášek, J. Krejčí, L. Fujcik, "Graphite pastes in thick film sensors area", Dubrovnik, 2003, ISBN 953-7124-00-2.

[2] BVT Technologies, a.s.: web pages, available at <http://www.bvt.cz>.

[3] F. Vydra, K. Šťulík, E. Juláková, "Rozpouštěcí polarografie a voltametrie", SNTL, Praha 1977

[4] M. Lanz, D. Schürch, G. Calzaferri, "Photocatalytic oxidation of water to O_2 on AgCl-coated electrodes", Journal of Photochemistry and Photobiology A: Chemistry 120 (1999) 105-117, Elsevier, 1999.

Modeling, Parameter Extraction and Simulation of a-Si:H Thin Film Transistors

L. Resendiz[1], M. Estrada[1], A. Cerdeira[1] and B. Iniguez[2]

[1]Sección de Electrónica del Estado Sólido (SEES), Departamento de Ingeniería Eléctrica CINVESTAV, Av. IPN 2508
Apto. Postal 14-740, 07300 D.F., México, E-mail: lresendiz@ieee.org
[2]Departament dÉnginyeria Electrónica Electrica i Automatica, Universitat Rovira i Virgili, 43007 Tarragona, Spain.

Abstract

In this paper we present a new procedure to determine subthreshold a-Si:H TFTs. The main characteristics of extraction procedure is the use of integral function, that permits to extract in a simple and direct way basic model parameters from experimental transfer and output characteristics. Other parameters required for device modeling in the sub and above threshold regimes are also determined. We report results of comparing calculated, using parameter values obtained with our new extraction procedure, simulated in AIMSpice a-Si:H TFTs after including the new subthreshold model, with experimental curves in all working regions of the devices. The validity of the procedure is tested for a-Si:H TFTs with channel length down to 4 μm.

1. Introduction

The basic model to simulate the behavior of hydrogenated amorphous silicon transistors (a-Si:H TFT) was developed and was later implemented in AIM-Spice level 15 model [1]. The number of parameters requested by this model is high. Parameters related to the above threshold regime can be extracted using a previous procedure reported by us [2]. Others, related to the trap distribution and intrinsic layer impurity concentration as the Fermi level position, E_{Fi}; the minimum density of deep states, g_{F0}, and the characteristic temperature of deep states T_2 have been estimated up to now.

In this article we report a new procedure to extract amorphous TFTs subthreshold model parameters. The minimum density of deep states g_{F0} and the characteristic temperature T_2 of the deep states of a-Si:H TFT are determined in a simple and direct way from the experimental measurements with no need of assigning predetermined values to any other model parameter. The other parameters required for modeling the subthreshold region are also extracted from experimental curves.

New level 25 in AIM-Spice was prepared, modifying model in level 15 where the expressions used to model mobility in the subthreshold region were substituted by the new ones.

The new level 25 was tested for a-Si:H TFTs with channel lengths down to 4 μm, showing good coincidence between simulated, using parameter values obtained with our new extraction procedure and experimental curves, in all working regions of the devices.

2.Basic Subthreshold Model Equations.

In subthreshold regime, drain current can be calculated as [3]

$$I_{DS} = K \cdot \left[\frac{(V_{GS} - V_{FB})^{\gamma_b}}{V_{bb}^{\gamma_b}} \right] \cdot (V_{GS} - V_{FB}) \cdot V_{DS} \qquad (1)$$

where

$$\gamma_b = \left(\frac{2T_2}{T} - 2 \right) \qquad (2)$$

and

$$V_{bb} = \frac{1}{C_{diel}} \left[\frac{1}{q \cdot f(T, T_2)} \right]^{\frac{1}{\gamma_b}} \qquad (3)$$

where

$$f(T,T_2) = \frac{N_C \cdot e^{\left(-\frac{E_C - E_{F0}}{kT}\right)} \cdot \frac{kT}{q}}{(\varepsilon_0 k_{Si})^{\frac{T_2}{T}-1}} \left[\frac{\cdot \sin\left(\frac{\pi T}{T_2}\right)}{2\pi \left(\frac{k^2 T_2 T}{q}\right) \cdot g_{F0}} \right]^{T_2/T} \qquad (4)$$

These expressions were introduced in AIM-spice simulator in order to model the subtheshold region of a-Si:H TFTs [4]

3. Results

Two a-Si:H TFTs one with W= 50 μm and L=12 μm and another with W=25 μm and L=4 μm were used to test the new subthreshold and extraction parameter method. The technological data for both devices was Si_3N_4 gate thickness of 410 nm; intrinsic layer thickness of 300 nm.

The band mobility parameter μ_0 was taken equal to its default value, 10 cm^2/Vs and E_{F0} = 0.68 eV.

Measured transfer and output I-V characteristics were used to extract the values of the model parameters [4], which serve as input parameters to the simulator. All model parameters were obtained using the method described in [3].

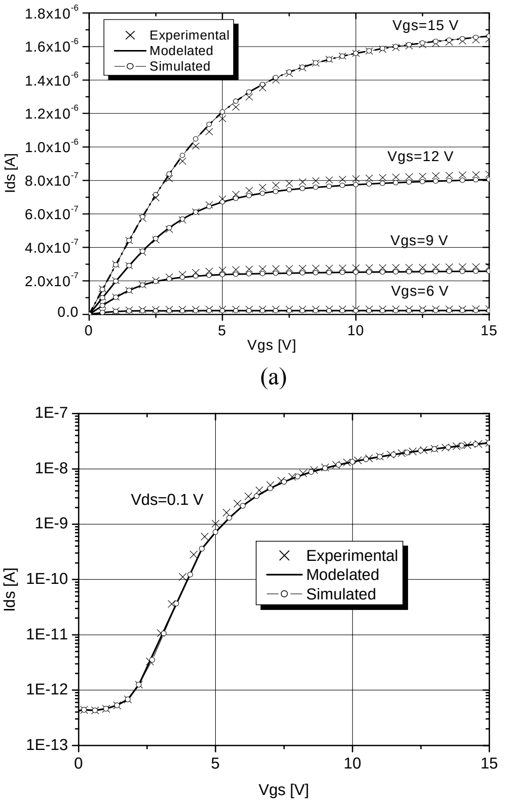

(a)

(b)

Fig.1. Comparison between experiment, modelated and simulated a) output, b) transfer; characteristics. W=50 µm L=12 µm

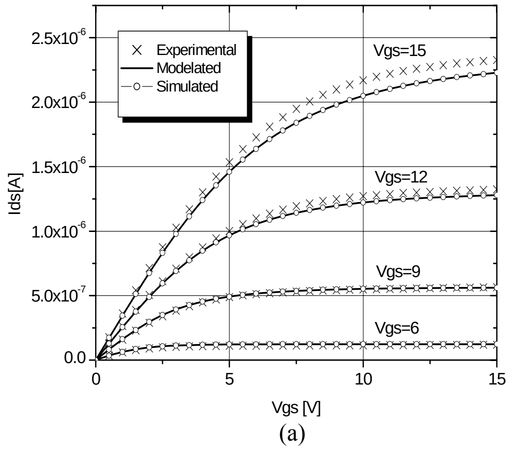

(a)

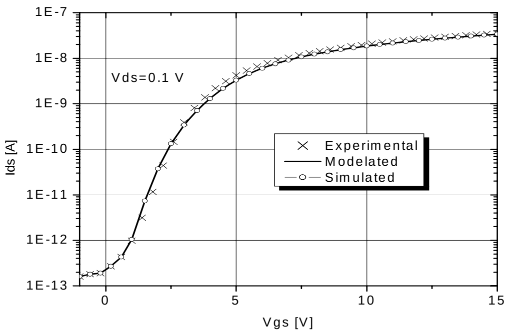

(b)

Fig.2. Comparison between experiment, modelated and simulated a) output, b) transfer; characteristics. W=25 µm L=4 µm

Figs 1 and 2 show the comparison between simulated, modelated and experimental curves, in all working regions of the devices.

4. Conclusions

A new procedure is presented to extract sub-threshold parameters of a-Si:H TFTs directly from the experimental output and transfer curves.

Using an integral method, the values of VFB, the characteristic temperature of the deep states and the concentration of deep states can be extracted independently one from the other using simple mathematical processing. No graphical methods or non-lineal optimisation are needed to calculate any of the parameters.

A new expression for the mobility in the sub-threshold region of a-Si:H TFTs was introduced in AIM-spice simulator. Comparison of experimental IDS-VGS and IDS-VDS with calculated, and simulated transfer and output curves using model expressions for a-Si:H TFTs with channel length down to 4 µm shows very good results, thus, validating the procedure.

Acknowledgements

This work has been supported by CONACYT project 3440A

References

[1] AIM-Spice, Circuit Simulation Program by AIM-Software (www.aimspice.com).

[2] A. Cerdeira, M. Estrada, R. Garcia, A. Ortiz-Conde, F. J. Garcia Sánchez, “New procedure for the extraction of basic a-Si:H TFT model parameters in the linear and saturation region”, Solid State Electronics, 2001, (45), 1077.

[3] L. Reséndiz, M. Estrada, A. Cerdeira, “New procedure for the extraction of a-Si:H TFTs parameters in the subtreshold region”, Solid State Electronics, 2003, (47), 1351.

[4] L. Reséndiz, B. Iñiguez, M. Estrada, A. Cerdeira, “Modification of amorphous level 15 AIM Spice model to include new subthreshold model” Proc. MIEL 2004, vol 1, pp.291-294.

Fabrication of Nb-doped Titania nanopawders by Sol-Gel route.

Edgar Sotter[1], Jan Prášek[2], Martin Adámek[2], Xavier Vilanova[1]

[1.] Dept. Enginyeria Electrònica Elèctrica i Automàtica, Universitat Rovira i Virgili
Avd. Països Catalans, 26, 43007 Tarragona. Phone: +34 977 558502, Fax: +34 977 559605,
E-mail: esotter@etse.urv.es
[2.] Dept. of Microelectronics, Technical University of Brno, Údolní 53, 602 00 BRNO, Czech Republic.

Abstract

Titanium dioxioxide doped with Niobium was synthesized by sol-gel route from alkoxide precursors. The gel obtained was dried to get the nanopowders and then calcined at various temperatures. Three different concentration of Nb doping has been made: 0.05 wt%, 0,2 wt% and 0,4 wt%.

1. Introduction

Titanium dioxide is widely used for oxygen detection in semiconductor gas sensors [1]. When this material is doped with pentavalent impurity ions, i.e. Nb^{5+}, it shows higher sensitivity towards oxygen gas and shorter response time than pure TiO_2 [2]. The doped material also shows low impedance and hence it is easier to design associated electronic circuitry [3,4].

This work reports the fabrication of Nb-doped titania nanopowders to be used in thick film oxygen sensors. Sol-gel method was chosen for the synthesis because of the low cost production facilities and the range of flexible chemical components.

2. Sol-gel synthesis

Nb-doped titanium was prepared from alkoxides precursors via sol-gel route in dry nitrogen atmosphere. The precursors used were titanium isopropoxide (IV) $Ti[OCH(CH_3)_2]_3$ 99,99% purity and niobium ethoxide $Nb(OC_2H_5)_5$ 99,99% purity. It was made a solution of these two precursors, in proper concentrations for doping, in isopropanol solvent. Then this solution was added to water containing nitric acid under stirring. The final composition of the constituents was set to satisfy $[Ti]:[HNO_3]:[H_2O]$ = 1:1:100 in molar ratio. The initial water concentration will be the main factor in average particle size. If it increases, it produces higher nucleation rates, which results in a decrease in average particle size. Based on this, a $[H_2O]:[Ti]$ ratio of 100 was selected. In the presence of such amount of nitric acid, the hydrolysis proceeded without forming a precipitate, giving rise to a transparent sol. Gellification of the sol was achieved by increasing the pH. This was done by adding a weak alkaline solution, i. e., an aqueous solution (1M) of Ammonium Carbonate [5].

3. Dried and calcinations process

The gel was dried at a temperature of 120ºC for 24 hours to eliminate organic elements. The obtained precipitate material was milled and then calcined at 600ºC, 700ºC y 800ºC.

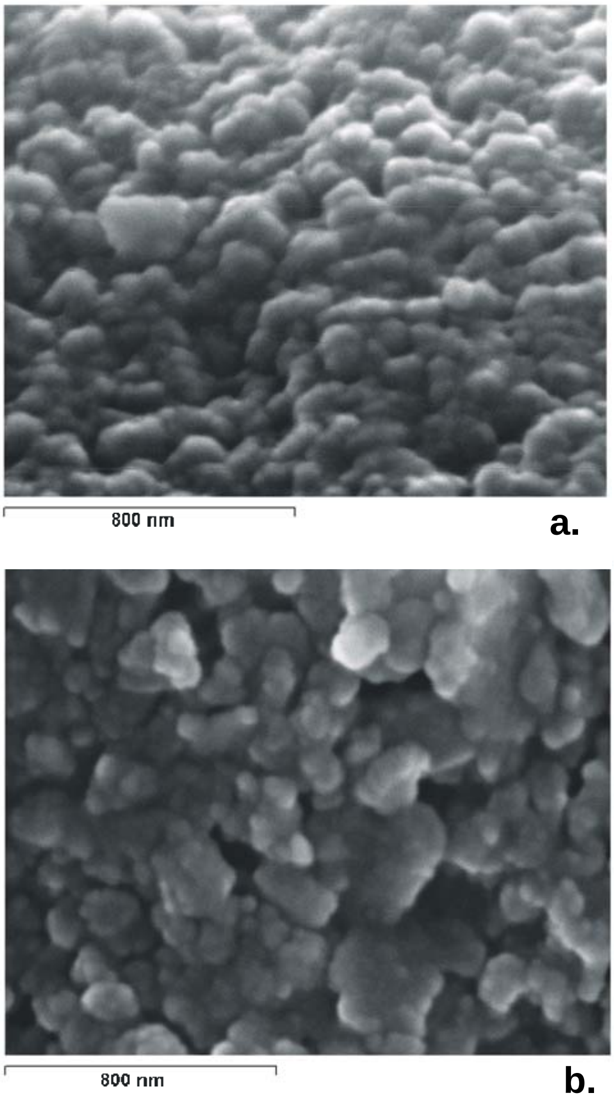

Figure 1. SEM micrograph of **a.**TiO_2 pure. **b.**TiO_2 doped with 0,05 wt% Nb.

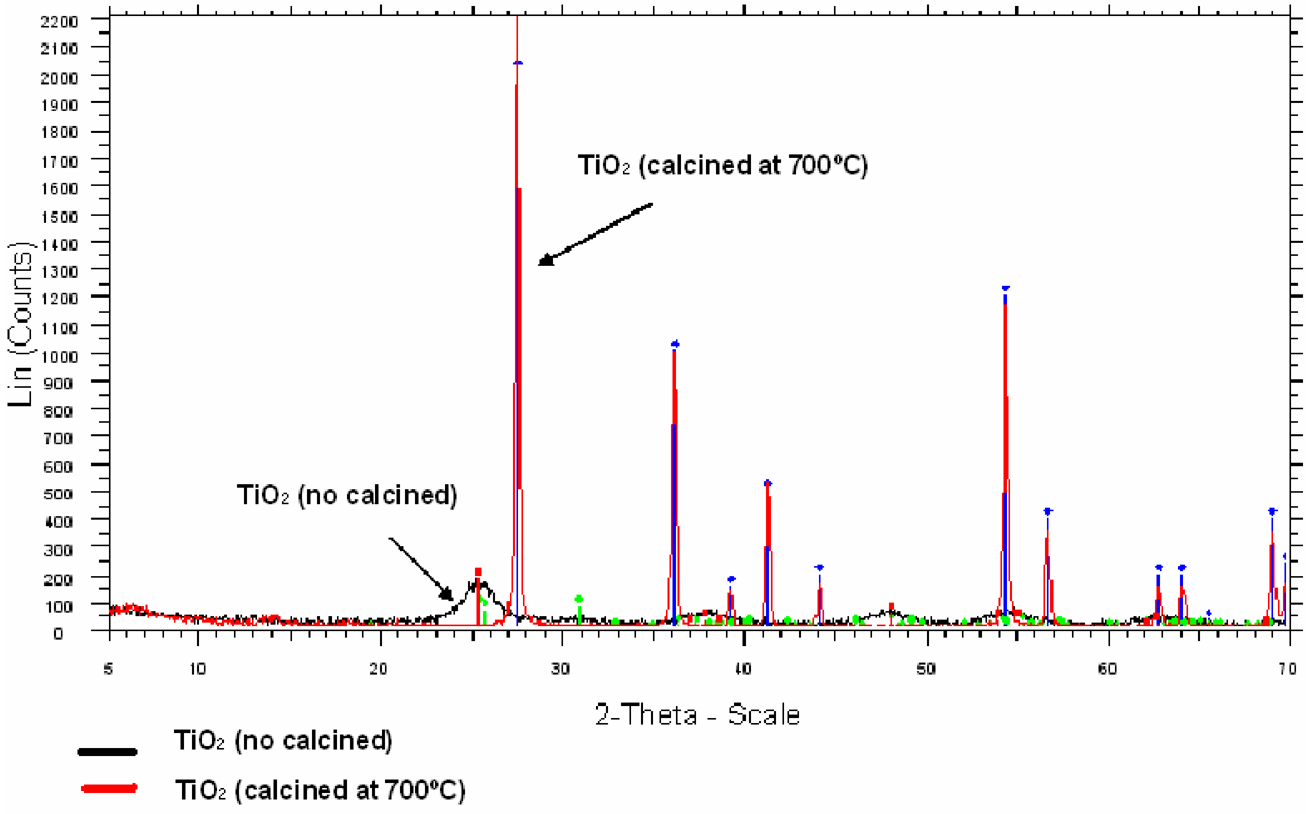

Figure 2. XRD patterns of TiO_2. Before calcinations (anatase state) and after 700ºC calcinations (rutile state).

4. Conclusions

Nb-doped nanopowders were made by sol-gel route. At the moment, SEM and XRD characterization of nanopowders are being made. First XRD results shows that grain growth of TiO_2 crystallites is hindered by the addition of Nb. This observation is also supported by SEM photographs, as shown in Figure 1; here it is possible to see a grain size of 60 – 100 nm approximately.

Change of phase of TiO_2 from anatase state to rutile state use to be over 600ºC [5]. First XRD results confirms the change of phase of TiO_2 from anatase state before any temperature treatment to rutile state after be calcined at 700ºC (Figure 2.). Further analysis will help to make a characterization of the behaviour of TiO_2 nanopawder structure under the increase of calcinations temperature.

ICP and AFM characterization will be made to verify the concentration of doping material and the grain size respectively.

Acknowledgements

We sincerely thank Dra. Ana Ruíz (Universidad de Barcelona) for her valuable technical assistance in the sol-gel process.

References

[1] U. Kiner, K.D. Schierbaum, W. Göpel. "Low and High Temperatura TiO_2 Oxygen Sensors". Sensors and Actuators B1 (1990) 103-107.

[2] R.K. Sharma, M.C. Bhatnagar, G.L. Sharma, "Effect of Nb metal ion in TiO_2 oxygen gas sensor", Applied surface science 92 (1996) 647 – 650.

[3] R.K. Sharma, M.C. Bhatnagar, G.L. Sharma, "Mechanism in Nb doped titania oxygen gas sensor", Sensor and Actators B 46 (1998) 194 – 201.

[4] A. Takami, "Develoment of titania heated exhaust gas oxygen sensor", Ceram. Bull. 67 (12) (1998) 1956 – 1960.

[5] A. Ruiz. "TiO_2 nanoparticles for gas sensor applications". Universitat de Barcelona, Departament d'Electrónica. 2003.

Resonant Grating Waveguide Structures for Two Photon Fluorescence Excitation

A.Thayil Karunakaran Nair, S. Soria, T. Katchalski[1], A.A. Friesem[1]

ICFO - Institut de Ciències Fotòniques, 08034 Barcelona, Spain. T.+34 93 4137944, F. +34 93 4137943.
anisha.thayil@icfo.es, silvia.soria@icfo.es
[1]Department of Physics of Complex Systems, Weizmann Institute of Science, 76100 Rehovot, Israel.

Abstract

An ultra sensitive method for Two Photon Fluorescence (TPF) excitation using resonant Grating Waveguide Structures (GWS) has been demonstrated. The enormous optical field enhancement that can be achieved on the grating surface is exploited for TPF spectroscopy, without the need for a highly intense, focused laser light. We present the enhanced TPF signal obtained from a drop of tetramethylrhodamine on the top of high-finesse resonant polymeric GWS. The results clearly indicate the detection sensitivity of the method down to picomolar concentration of the dye molecules.

1. Introduction

Two Photon Excitation (TPE) has been extensively applied in a variety of fields like laser scanning microscopy and fluorescence spectroscopy [1]. The main advantage of TPE is the easy spectral separation of the excitation radiation from the induced fluorescence thereby providing substantially background free detection on a single molecular level. Significantly lower autofluorescence and a larger tolerance of the cells and tissues to near infrared radiation make TPF a powerful tool in the study of biological systems and processes.

However, conventional TPE requires high photon densities in excess of at least 10^5W/cm^2 so the photodamege threshold is lowered. In order to avoid the use of highly intense focused laser light, we resort to resonant devices based on grating waveguide structures (GWS). In its basic configuration, a GWS is a multilayer stack consisting of a substrate, a waveguide and a grating layer on the top. At a specific wavelength and angular orientation of the incident beam a resonance occurs so that most of the incident light is reflected. Specifically, a very sharp dip occurs in the spectrum of the illuminating pulse [2]. This abnormal reflection brings out an enormous optical field enhancement at the grating surface which can be exploited for TPE of a layer that is deposited on the top of grating.

We present some of the representative results of TPF with tetramethylrhodamine (TMR) molecules immobilized on the grating layer, at and off resonance. Following the preliminary results obtained from the combination of polymeric GWS with a dried drop of 1.5µM TMR solution [3], we tested the detection sensitivity still at lower concentration levels.

2. Experimental Method

To fabricate the GWS, a polyimide layer of thickness 430 nm (refractive index 1.7) and a layer of Shipley S1805 photoresist were spun coated on an optical quality glass substrate. A grating layer of thickness 450 nm with a period of about 523 nm was holographically recorded on to the photoresist layer. The grating structures were optimized to minimize surface roughness and achieve high uniformity. Afterwards a drop of 23 nM TMR solution in milli-Q water (pH=7.5) was deposited on the top of GWS. After evaporation of the solvent, the TMR molecules remained immobilized on the top the grating. In order to check the detection sensitivity still at a lower concentration, a drop of 2.3 pM TMR was deposited on another GWS with the same configuration.

The experimental arrangement for the evaluation of TPF together with a GWS configuration consisted of a mode-locked Ti: Sapphire laser (Coherent) operated at a frequency of 80 MHz. The pulse width was 140 fs and the spectral bandwidth was 8 nm. The GWS was mounted on a positioning stage (Physik Instrumente) to ensure normal incidence, for which the GWS was designed. Laser beam of maximum average power 360 mW was slightly focussed to a 100µm beam waist, using a lens of f = 20 cm. The TPF was collected by a microscope objective lens (20×, NA=0.46) and was focussed onto the entrance slit of a spectrometer (Jobin Ivon). A back thinned CCD linear array (Hamamatsu) was used for the signal detection. A NIR filter (BG39, Schott) was placed in front of the entrance slit of the spectrometer to block the excitation light.

3. Results and discussion

The resonant behaviour of the grating waveguide structures was tested for normal incidence with transverse electric (TE) polarization illumination (the electric field of the incident light is parallel to the grating grooves). Figure 1 shows the transmission spectra of the combination of GWS with a 10µl drop of 23nM TMR. As expected, the transmission spectral profile has a dip at the resonant wavelength λ_{res}= 826.6nm with a full width at half maximum (FWHM) of 1nm. The transmission intensity drops almost 70% at the resonance wavelength.

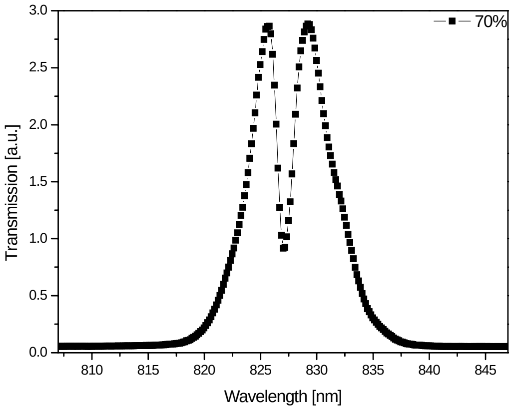

Fig.1. Spectral response of the combination of GWS with a dried drop of 23 nM TMR on its top.

Figure 2 shows the TPF spectra as a function of wavelength for different excitation wavelengths. There is very low background fluorescence at wavelengths away from resonance. Close to resonance, strong enhancement of TPF intensity with its maximum at 826.6nm clearly indicates that the fluorescence is due to the GWS. For transverse magnetic (TM) polarization mode at 826.6nm, TPF is in the background level.

Finally we repeated the measurements with a dried drop of TMR solution of 2.3 pM concentration onto the GWS. Resonance wavelength in this case was at λres=828.6nm with only 25 % of reduction in the transmission intensity. As evident form Fig.3, TPF enhancement occurs only at excitation close to the resonant wavelength with its maximum coinciding with λres. The noise level of the TPF signal in this case is higher owing to the lower concentration of the dye molecules and the low resonance.

We observed a second order dependence of the fluorescence intensity on the excitation intensity which confirms the two photon character of the emitted fluorescence. TPF enhancement was found to be higher for GWS with a better resonance indicating the field enhancement at the grating surface is responsible for the observed fluorescence. In this case, the signal to noise ratio decreases.

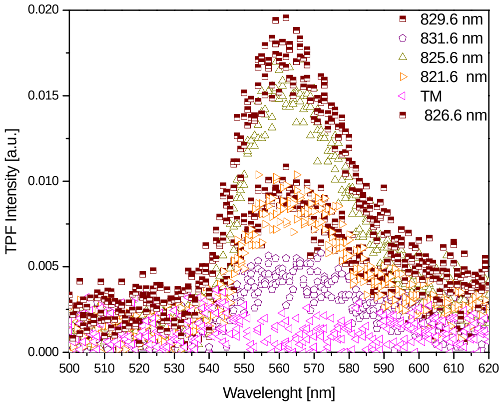

Fig.2. TPF spectra of TMR (23×10^{-9} M in water) with GWS (λ_{res}=826.6nm) at and off resonance excitation wavelengths and also for TM polarization illumination

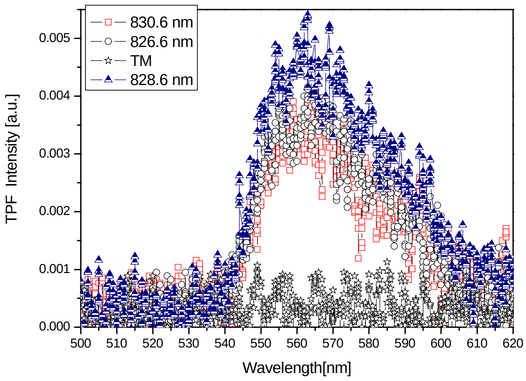

Fig.3. Two Photon Fluorescence spectra of TMR molecules with GWS(λ_{res}=828.6nm) for different excitation wavelengths. Concentration of the deposited TMR sample was 2.3×10^{-12} M.

4. Conclusions

Enhancement of Two Photon Fluorescence of the immobilized TMR molecules using resonant GWS has been described. A detection limit up to pico molar concentration of the dye molecule has been achieved offering the possibility of a highly sensitive, compact and non-destructive tool for widespread biological and chemical applications

References

[1] W.Denk, J.H. Strickler, W. W. Web, "Two –photon laser scanning microscopy", Science, pp.73-76, Apr 1990.

[2] D.Rosenblatt, A. Sharon, A.A.Friesem, "Resonant Grating Waveguide Structures",IEEE Journal of Quantum Electronics, pp.2038-2059, Nov 1997.

[3] S. Soria ,T.Katchalski,E. Teitelbaum, A.A Friesem G. Marowsky,"Enhanced Two-Photon Fluorescence Excitation by Resonant Grating Waveguide structures", Optics Letters, 2004(in press)

Fabrication of Silicon Oxide Microneedles from Macroporous Silicon

E. Valera, D. Molinero, A. Rodriguez and R. Alcubilla
Departament d'Enginyeria Electrònica, Universitat Politècnica de Catalunya
C/ Jordi Girona 1-3 Campus Nord, 08034 Barcelona, Spain

T. Trifonov, L. Marsal and J. Pallarès
Departament d'Enginyeria Electrònica, Elèctrica i Automàtica, ETSE, Universitat Rovira i Virgili
Campus Sescelades, Avda. Països Catalans 26, 43007 Tarragona, Spain

Abstract

This work presents a novel technique for silicon dioxide microneedles fabrication. Microneedles are hollow microcapillaries with tip diameters in the range of micrometers allowing the fabrication of micro-syringes. These structures are interesting in medical and biological applications, such as DNA injection, antibody manipulation and delivery, and cell manipulation. The silicon dioxide at the tip of microcapillaries is etched in buffered hydrofluoric acid. In this work microneedles arrays have been fabricated with pore diameters in the range of 2-5µm, with lengths from 30-140µm and 70 nm thick walls.

Keywords.- microneedles, macroporous silicon, electrochemical etching, bio-applications.

1. Introduction

Macropore fabrication by means of electrochemical etching (ECE) in optional designs predetermined by photolithography is known since 1990. Since then, new devices and materials based on this electrochemical process have been developed [1]. Recently, lot of attention has been paid to bio-applications of micromachining technology [2]. By combining these technologies, we have fabricated microneedles, with potential applications in the chemical and biomedical fields as fluid delivery or precisely located chemical-reaction stimulation.

2. Fabrication Process

The microneedles fabrication is based on macropore formation. The macropore formation on n-type silicon wafer <100> with resistivity of 1-10 ohm-cm, is performed by photoassisted electrochemical etching (ECE) in low concentration hydrofluoric acid. For the electrochemical etching we use a special Teflon set-up, whose scheme is showed in the Figure 1.

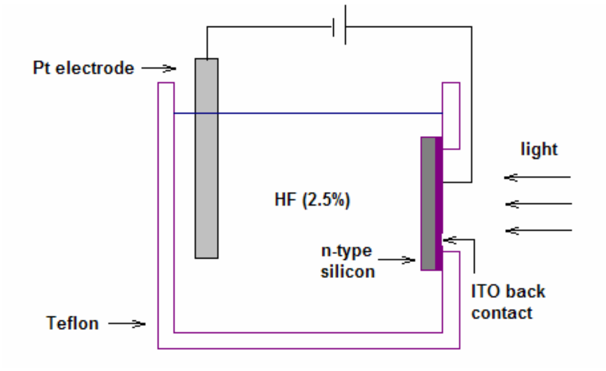

Fig.1. Scheme of the electrochemical etching set-up.

Using lithographical patterns the distance between pores can be defined. Microneedles morphology depends on the anodization conditions such as current density, etching time, HF concentration, temperature, bias as well as on substrate properties: doping density and orientation. Afterwards formation, the etched macropores were oxidized and the microcapillaries were released using backside TMAH etching [3]. Silicon oxide at the tip of microcapillaries was etched in buffered hydrofluoric acid.

The fabrication sequence is as follows:

1. Wafer oxidation.
2. SiO_2 lithography.
3. Silicon etch in TMAH.
4. Backside ITO deposition.
5. Macroporous silicon formation.
6. Wafer cleaning.
7. Microporous silicon etch in TMAH.
8. Silicon dioxide growth.
9. Backside lithography.
10. Silicon etch in TMAH, until tips are reached
11. Tip opening by oxide etching in buffered HF.
12. Silicon etch in TMAH.

This sequence is also outlined schematically in Figure 2.

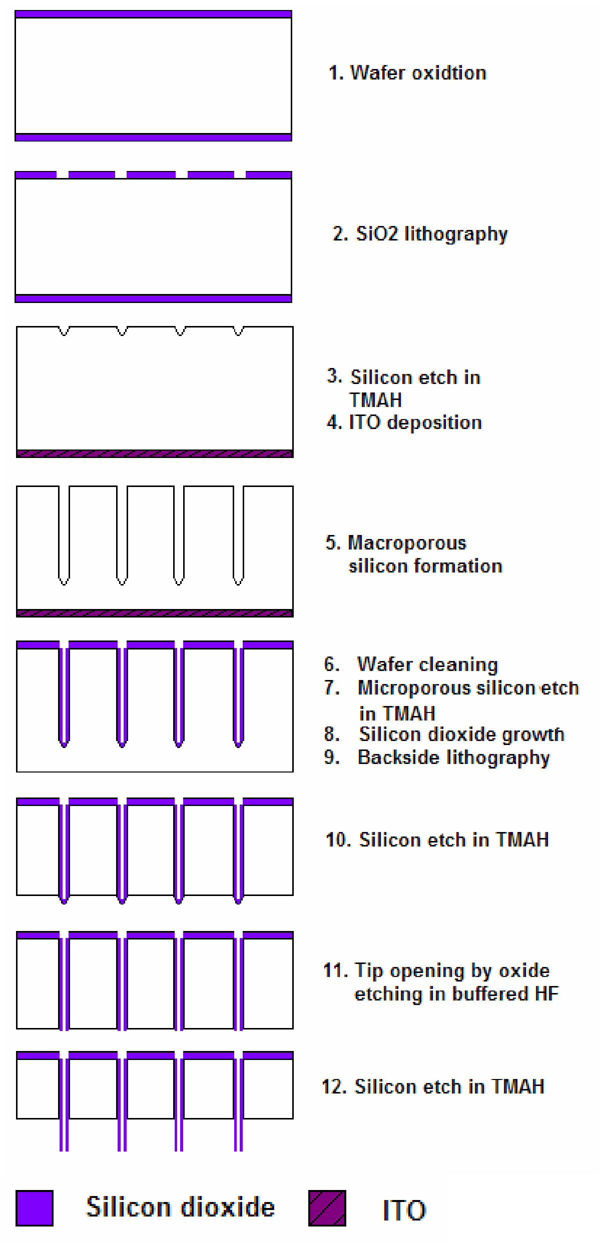

Fig.2. Process flow for microneedles fabrication.

3. Results

Microneedles can be fabricated by this method with diameters ranging from less than 1µm to several tens of microns. In this work microneedles arrays were fabricated with pore diameters in the range of 2-5µm, with lengths from 30-140µm and 70nm thick walls. Microneedles inner diameter can be further adjusted by controlling the thickness of SiO_2 on the walls. In this way inner diameters in the submicron range can be obtained.
Figure 4 shows the top view of an array of microneedles, and Figure 5 shows a lateral view of a group of microneedles. The length of these structures is 50µm, and the pore diameter is 2µm.

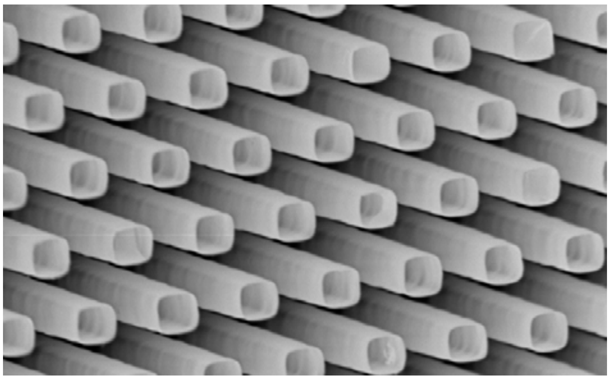

Fig.4. SEM picture of top view of an array of microneedles.

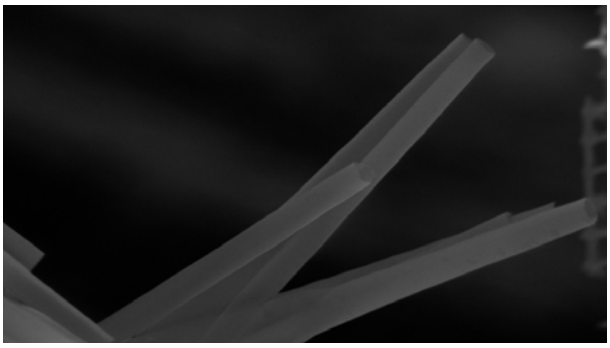

Fig.5. SEM picture of lateral view of an array of microneedles.

4. Conclusions

A novel technique for silicon dioxide microneedles fabrication, based on macroporous silicon is described. Using this technology we have fabricated, microneedles arrays with different geometries, with lengths and pore diameters, ranging between 30-140µm and 2-5µm respectively. Additionally, our process allows to modulate the microneedles thickness. Inner diameter of the resulting structures can be also adjusted controlling the thickness of the oxide layer. Tubes with submicron inner diameters can be easily formed using this technique.

References

[1] V. Lehman, U. Grüning “The limits of macropore array fabrication”, Thin Solid Films 297, pp. 13-17, 1999.
[2] K. Chun, G. Hashiguchi, H. Toshiyoshi, H. Fujita, Y. Kikuchi, J. Ishikawa, Y. Murakami, E. Tamiya “An Array of Hollow Microcapillaries for The Controlled Injection of Genetic Materials into Animal/Plant Cells”, IEEE pp. 406-411, 1999.
[3] T. Trifonov, A. Rodríguez, F. Servera, L. F. Marsal1, J. Pallarès and R. Alcubilla “High-aspect-ratio silicon dioxide pillars”, Porous Semiconductors - Science and Technology, Cullera, Valencia, 2004.

Optimised Temperature Modulation of Metal Oxide Micro-Hotplates Gas Sensors through Multi-Level PRS

A. Vergara[1], E. Llobet[1], J. Brezmes[1], P. Ivanov[1], X. Vilanova[1], I. Gracia[2], C. Cané[2], X. Correig[1].
[1] Dept. Electronic Engineering, URV, Tarragona, Spain,
[2] Dept. Microsystems and Silicon Technologies, CNM, Barcelona, Spain

Abstract

A method based on multi-level pseudo-random sequences (PRS) for modulating the working temperature of metal oxide micro-hotplate gas sensors in a wide frequency range is defined. In addition to reducing the effects of noise and non-linearity, this method helps in identifying each gas-sensor/system and in finding those modulation frequencies important for discriminating and quantifying different gases.

1 Introduction

Although metal oxide gas sensors are inexpensive and very sensitive to different toxic species, they still suffer from serious shortcomings such as poor selectivity and response drift.

Among the different strategies used to improve selectivity and fight drift, the modulation of the operating temperature of gas sensors has been remarkably successful in many applications [1]. Although the results reached were very promising, the selection of the modulation frequencies used in previous works were based on a trial and error procedure, and there was no way to ensure that these modulation frequencies were the optimal for a given application.

In a previous work [2], we reported a systematic method to choose the modulation frequencies of micro-hotplate gas-sensors based on MLS pseudo-random binary sequences.

In the present paper, a new method to modulate the working temperature of metal oxide micro-hotplate gas sensors in a wide frequency range is presented, based on maximum length multi-level PRS instead of the binary signals. One of the main reasons for considering multilevel signals is that they can provide a better estimate than binary signals of the linear dynamics of a process with non-linearities (chemical sensing) and they can also be used in the identification of the non-linear characteristics themselves. This method enables each gas-sensor system to be identified and to find, in a systematic way, those modulation frequencies that are important to discriminate between different gases and to estimate gas concentration.

2. Integrated micro sensor array

The integrated micro-hotplates with arrays of 4 micro sensors were fabricated on double-side polished p-type <1 0 0> Si substrates, 300 μm thick [3]. The structure of the devices basically consists of a gas-sensing layer, the electrodes, insulating layers and a polysilicon heater. The active layers were nano-particle WO_3 deposited by screen-printing.

3. Multi-level pseudo-random signals

Fig.1. Multi-level PRS generation algorithm

The theory behind the generation of m-level PRS inputs for system identification is well developed.

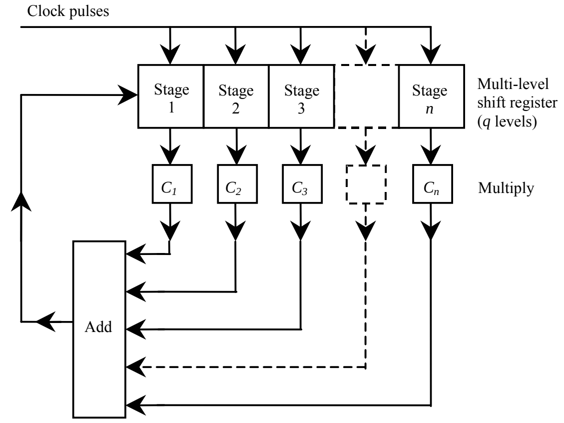

As in binary PRS, m-level PRS signals are periodic, deterministic signals, and have an autocorrelation function similar to white noise. M-level PRS exist for the number of levels, q, equal to a prime or a power of a prime p(>1), i.e. for q = 2, 3, 4, 5, 7, 8, 9, 11, 13, ... (Zierler, 1959), [4]. The length of such a sequence $\{x_r\}$ is $q^n - 1$, where n is an integer. M-level PRS signals are generated in a similar manner that the PRBS using a shift register and modulo addition. Figure 1 shows the shift register configuration for m-level PRS generation, where we can see that $\{x_r\}$ are integers 0, 1, ..., (q - 1). The sequence can be thought of as being generated by a q-level shift register with feedback to the first stage consisting of the modulo q sum of the outputs of the other stages multiplied by coefficients c_1, ..., c_n which are the integers 0, 1, ..., (q - 1).

4. Results and discussion.

An estimate of the impulse response, $h(t)$, of each sensor in the presence of pollutant gases was computed through the circular cross-correlation of one period (L = 624 samples) of the m-level PRS signal, $x(t)$, and one period of the sensor response (i.e. resistance transient), $y(t)$. The clock frequency of the m-level PRS was set to fc = 2 Hz and the sampling rate of the acquisition system was set to 10 Hz.

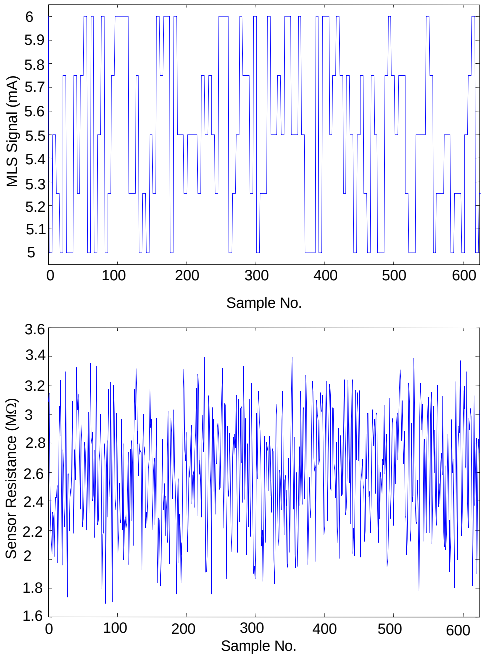

Fig. 2. M-level PRS applied to the heater element (top) and resulting resistance of a WO_3 micro-hotplate sensor in the presence of 2 ppm of NO_2 (bottom).

Vapours of 3 different concentration of NO_2 (0.5, 1, 2 ppm) and NH_3 (100, 500, 1000 ppm) and theirs binary mixtures diluted in dry air were measured while modulating the working temperature of the micro-hotplates. Each measurement was replicated 8 times. Five of these replicates per gas and concentration (30 measurements) were employed to find and select the modulation frequencies for gas identification and quantification (selection set). The remaining 18 measurements were used to validate the modulation frequencies selected (validation set). Figure 2 shows the m-level PRS signals used to modulate the sensor temperature and a typical response of micro-hotplate gas sensor.

The sequences were decimated by 5 before the cross-correlation was computed. The absolute value of the fast Fourier (FFT) of the impulse response estimate was calculated and stored for further processing. Figure 3 shows the absolute FFT value of the impulse response estimate of the WO_3 micro-hotplate gas sensor in the presence of NH_3 and NO_2 where we can see the differences that exist between these two spectra. A selection process was implemented to determine those spectral components that were important for identifying and quantifying the gases.

One matrix per sensor was formed with the spectral components selected from the selection set. These matrices were then used to build and validate fuzzy ARTMAP classifiers in order to see whether it was possible to correctly identify and quantify the gases. A cross-validation of order one was implemented to estimate the success rates for gas identification, which varied between 78 to 98 % using a single sensor.

On the other hand the success rate was up to 87 % when quantifying NH_3 and NO_2 and up to 93 % when quantifying mixtures gas, using only one sensor, and up to 100 % combining sensors.

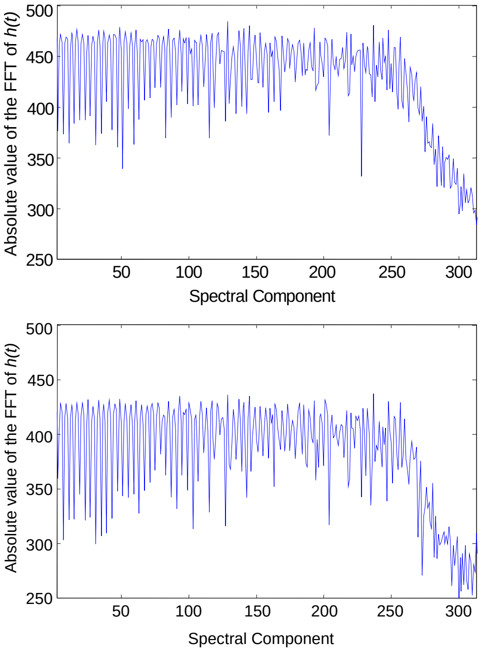

Fig. 3. Absolute value of the FFT of h(t) for WO_3 micro-hotplate in: 1000 ppm NH_3 (top) and 2 ppm NO_2 (bottom).

The procedure of frequency selection was validated with the 18 remaining measurements (validation set). In gas identification the success rate was near 90%. These results with an independent validation set prove the validity of using m-level PRS signals to optimise the set of modulating frequencies that should be used for a given gas analysis problem.

References

[1] E. Llobet, J. Brezmes, R. Ionescu, X. Vilanova, S. Al-Khalifa, J.W.Gardner, N. Bârsan and X. Correig; Sensors and Actuators B, 83, 2002, pp 238-244.

[2] A.Vergara, E. Llobet, J. Brezmes, M. Stankova, P. Ivanov, X. Vilanova, I. Gràcia, C. Cané, X. Correig; Book of abstracts of IEEE sensors 2003, pp. 440-441, Toronto, Canada, October 2003.

[3] E. Llobet, P. Ivanov, X. Vilanova, J. Brezmes, J. Hubalek K. Malysz, I. Gracia, C. Cané, X. Correig; Sensors and Actuators B, 96, 2002, pp 94-104.

[4] K. Godfrey, Perturbation signals for system identification, Prentice Hall, UK, 1993.

Early detection of fungal growth in bakery products using an e-nose based on mass spectrometry

M. Vinaixa, J. Brezmes, E. Llobet, X. Vilanova, X. Correig.

DEEEA, Universitat Rovira i Virgili, Avda. Països Catalans, 26, 43007 Tarragona, Spain.

Abstract

This paper presents the evaluation of a SPME-MS based -e-nose device for early detection of unwanted fungal growth in bakery products. The proposed approach can detect fungal growth and predict fungal genre before visual detection.

Introduction

In recent years, consumers have shown a growing concern about quality and safety of food. The food industry needs the development of fast and simple techniques to trace the quality of raw materials and finished products. Microbial spoilage is a major problem in bakery products since it can induce nutritional losses, off-flavors and formation of mycotoxins or potentially allergenic spores. On the other hand, it is known that fungi produce volatile compounds during both primary and secondary metabolism. These volatiles can also be used as markers to detect food spoilage or unwanted fungal growth. Most of the studies on the detection and identification of volatile derived from fungal spoilage have been done using GC/MS. This implies the development of a chromatographic method to analyze the samples. This is a time consuming task that requires trained personnel and offers low sample throughput because of the time needed in a full resolved chromatographic run. Therefore, since the volatile headspace is complex and should be evaluated as a whole, techniques that mimic the human olfactory system (the so-called electronic noses) have already been proposed. Some e-nose techniques based on different types of non-specific sensors (i.e metal oxide, conducting polymer) have been evaluated in the detection of fungal, bacterial and yeast spoilage. Nevertheless, these systems suffer from serious drawbacks (drift, poor selectivity, poor repetitivity and low throughput) that prevent them from becoming useful tools when monitoring fungal growth in industrial applications. A more innovative e-nose approach based on solid phase microextraction, mass spectrometry and complex data processing algorithms overcomes many of these drawbacks. This paper presents the study of a SPME-MS based-e-nose to monitor unwanted fungal growth in bakery products.

2. Experimental

Experiment 1

The goal of the first experiment was to evaluate the usefulness ofa SPME-MS based -e-nose in a classification problem involving 8 different in-vitro growing fungal cultures (Aspergillus flavus, AF, Aspergillus niger, AN, Eurotium amstelodami, EA, Eurotium herbariorum, EH, Eurotium rubrum, EU, Eurotium repens, ER, and Penicillium corylophillum, PE) according their fungal genera or specie. Nine replicates of 0.90 aw slants of 2% wheat flour agar medium were prepared in 20-mL vials. Sampling of volatile headspace based on SPME was performed using a 75-µm Carboxen/PDMS fiber that was introduced into the vial and exposed to the headspace of fungal cultures for 20 min at room temperature. Thermal desorption of volatiles was conducted for 3 minutes at 300ºC in the chromatograph injection port of a Shimadzu QP 5000 GC/MS that was used to implement as MS e-nose. This GC/MS was equipped with a 5- m deactivated fused silica column to co-elute all volatiles without chromatographic separation. The column was kept isothermal at 250ºC and the helium flow was set to 1.4 ml/min. A fingerprint m/z pattern fragmentation was obtained averaging mass spectra along the single chromatographic peak. The fact that this pattern fragmentation was characteristic from each fungal culture allows us to distinguish them applying methods based on pattern recognition techniques.

Experiment 2

The second experiment was designed to simulate a real application. The aim was to evaluate the minimal period of inoculation time from which the SPME-MS-e-nose device was able to discriminate among vials with fungal growth and uninoculated vials. Genus discrimination was also attempted. Measures were performed on in-situ growing cultures over bakery product analogues. This is a much more realistic but difficult task since analogues can produce their own volatile pattern profiles; these volatiles produce additional signals in the mass detector that introduce noise into mathematical predictive model. Eight blank control vials containing cake analogues, eight replicate vials containing cake analogues inoculated with EA and four replicates innoculated with ER, EU, EH, AN, AF, and PE were measured. SPME extractions and MS- e-nose measurements were performed in every vial 24, 48, 72, 96 and 168 hours after inoculation as described above. Overall, 40 experimental points were obtained for each sampling time.

3. Results and discussion

3.1 Results on experiment 1

A total of 72 SPME-MS measurements were performed on in-vitro growing cultures. Figure 1 shows a score plot from the PCA performed on these measurements. Squares represent samples corresponding to Aspergillus genera, circles represent control blanks, crosses to Eurotium genera and Penicillium samples are represented by a downward triangle. It can bee seen that samples belonging to Aspergillus, Penicillium and Eurotium clustered together with low dispersion without overlapping with blank controls, which were clearly separated from the rest. Applying a DFA coupled to a Fuzzy Artmap neural network model allowed a 100% success rate when discriminating between fungal genera. Trying to classify samples according to their fungal species reached a 92% success rate; the model misclassified 7 measures out of 72. All failures were mistakes between species from Eurotium genus.

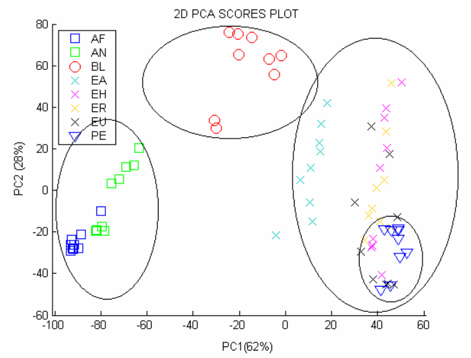

Fig.1. Scores plot from in-vitro fungal cultures.

3.2 Results on experiment 2

Table 1 summarizes success rates obtained on a cross-validated DFA coupled to a Fuzzy Artmap NN model at different incubation hours. Success rate on genus prediction of fungal cultures is low in the first stages of fungal growth, since the compounds produced in the highest amounts at early stages are similar for several species. Volatile compounds that might allow species classification are mainly produced during secondary metabolism probably after 48 hours of incubation when the system is able to predict fungal genera with a 78% success rate. Sporulation coinciding with visual detection happens 72-96 hours after inoculation depending on fungal spp. Sporulation leads to an increase in several volatile compounds generating different pattern profiles for each fungal genus or specie which allow the best discrimination results in our model. Contaminated and not contaminated samples can be clearly distinguished after 48 hours of incubation time, as it is shown in Figure 2. This is in good agreement with our prediction model that achieved a 98% success rate after 48 hours. Moreover, samples belonging to the same genus appear to cluster together, tendency that becomes more pronounced as the time of incubation increases. Again these results are in good agreement with our predictive model because after 48 hours the instrument achieved a 78% and 88% after 96 hours.

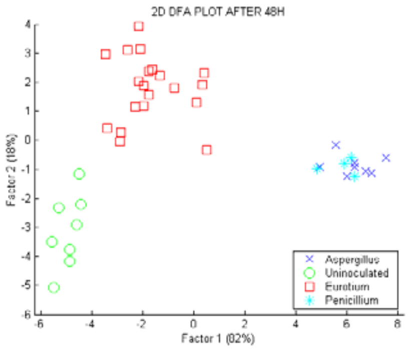

Fig.2. 2D DFA plot from in-situ fungal cultures after 48 hours.

Incubation hours	Discrimination among	Succes rate (%)
24	fungal growth	88
	genera	58
48	fungal growth	98
	genera	78
72	fungal growth	100
	genera	78
96	fungal growth	100
	genera	88
168	fungal growth	100
	genera	88

Table 1. Success rates of DFA-Fuzzy ARTMAP, measurement set along the first 168 incubation hours.

4. Conclusions

An SPME-MS based e-nose to monitor unwanted fungal growth in bakery products has been evaluated simulating real operating conditions. The instrument offers a fast alternative that can be easily automated and, therefore, operated. Since many QC departments already have GC-MS equipment, they can convert their units into a MS-based e-nose, coupling a SPME sampling system and using additional pattern recognition software. This configuration can make a measurement every 5 minutes leading to a fast detection system that can operate as a detection and diagnosis tool that allows near real time correction actions to be taken to the production chain, during storage and before any distribution of the product.

5. References

M. Vinaixa, S. Marín, J. Brezmes, E. Llobet, X. Vilanova, X. Correig. “Early detection of fungal growth in bakery products using an e-nose based on mass pectrometry”, J. Agric. Food Chem., submitted.

6. Acknowledgements

This work was founded by "Redes temáticas de investigacion cooperativa: RED DE CENTROS EN METABOLISMO Y NUTRICIÓN C03/08"

Applications of One-Dimensional Porous Silicon Photonic Crystals

E. Xifré Pérez*, J. Pallarès, J. Ferré-Borrull, and L.F. Marsal

Departament d'Enginyeria Electrònica, Elèctrica i Automàtica, ETSE, Campus Sescelades, Universitat Rovira i Virgili,
Avda. Països Catalans 26, 43007 Tarragona, Spain. *E-mail: exifre@etse.urv.es

Abstract

One-dimensional photonic crystals are useful for the fabrication of optical devices because of their peculiar optical properties, such as abnormal refractive index and gain enhancement at the band edge. The use of porous silicon for their fabrication opens up the possibility of easily adjusting the refractive index and the thickness of the layers for the best fitting to an application. We have theoretically studied some optical devices based on multilayers, specially for 1.55 μm applications, and we here discuss some of their characteristics and singularities.

1. Introduction

Photonic crystals are structures made of low-loss periodic dielectric media that posses photonic band gaps (PBG), that is, ranges of frequency in which light can not propagate through the structure. The simplest possible structure is the one-dimensional photonic crystal or multilayer.

A very attracting material for the fabrication of multilayers is porous silicon, which has attracted great interest because of the possibilities it offers to produce a new generation of both active and passive optoelectronic devices [1]. This material can be obtained by HF electrochemical etching of silicon, which generates a range of refractive indices by changing the current density during anodization process. The thickness is determined by the time during which the current is applied [2]. It has excellent mechanical and thermal properties and is obviously compatible with silicon-based microelectronics.

One-dimensional porous silicon photonic crystals are appropiate for many applications. In this paper we present some of the most important ones.

2. Porous silicon multilayer structure

One-dimensional photonic crystals are made of the periodic repetition of different refractive index layers. Each period consists of two porous silicon layers with refractive indices n_1 and n_2, and thickness h_1 and h_2, respectively, as it can be seen in Fig. 1.

The propagation of electromagnetic waves through a multilayer can be solved by the transfer matrix method [3] which permits the calculation of reflectance and transmission spectrum and the photonic band gap of layered media.

3. Applications

Although one-dimensional photonic crystals are very simple structures, they have many applications. Some of the most common are:

3.1.- Distributed Bragg Reflectors (DBR)

Distributed Bragg Reflectors are multilayers where the thickness of the two periodic layers is given by $n_1h_1= n_2h_2=\lambda/4$ [4]. This structure presents a high reflectance band centered at approximately λ. Figure 2a shows the reflectivity spectrum of a DBR with $\lambda=1.55$ μm, $n_1=2.4$ and $n_2=1.7$. It can be observed that when the number of periods N increases, the filter is more abrupt and the reflectivity inside the band gap tends to unity exponentially with N.

3.2.- Microcavities

These filters are generally obtained by inserting a defect layer in between two symmetric λ/4 Bragg reflectors. The optical thickness of the defect is usually λ/2 or λ.

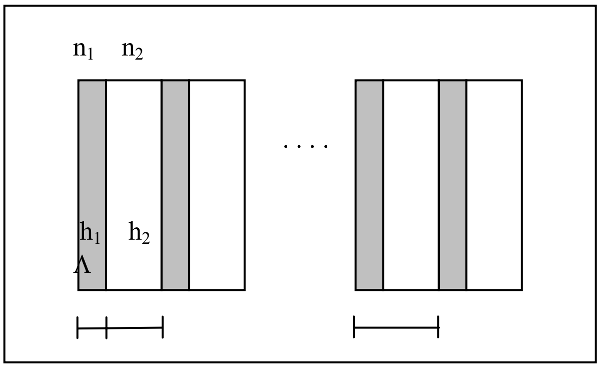

Fig.1. Schematic representation of a multilayer. Each period consists of two porous silicon layers with refractive index n_1 and n_2 and thickness h_1 and h_2, respectively. The period thickness is $\Lambda=h_1+h_2$.

The interference of the reflections of the two Bragg reflectors causes a maximum of transmission at λ between two spectral regions of high reflectance (band gaps) [5]. A microcavity for λ=1.55 μm can be observed in Fig. 2b. The reflectivity spectra show a transmission peak at λ, which is narrower when the number of periods N of the DBR increases.

This structure has potential applications in channel filtering within telecommunications devices with small insertion losses because the number and position of resonance peaks can be designed and their linewidths controlled in the NIR region.

3.3.- Omnidirectional mirrors

These multilayers reflect light at any polarization, at any incidence angle in specific wavelength regions. This property will allow the creation of all-optical integrated circuits as it can be used to confine, manipulate, and guide the photons [6]. The presence of an omnidirecional band gap depends on the ratio n_1/n_2 (the higher the ratio the wider the band gap) and on the ratio h_1/Λ. For every n_1/n_2 exists an optimum h_1/Λ ratio for which the omnidirectional band gap is maximum. Figure 3 shows the reflectivity spectra of an omnidirectional mirror for different angles of incidence. The band gap of the structure moves to lower wavelengths when the angle increases but there is a wavelength range where reflectivity is maximum for all incidence angles, that is the omnidirectional band gap.

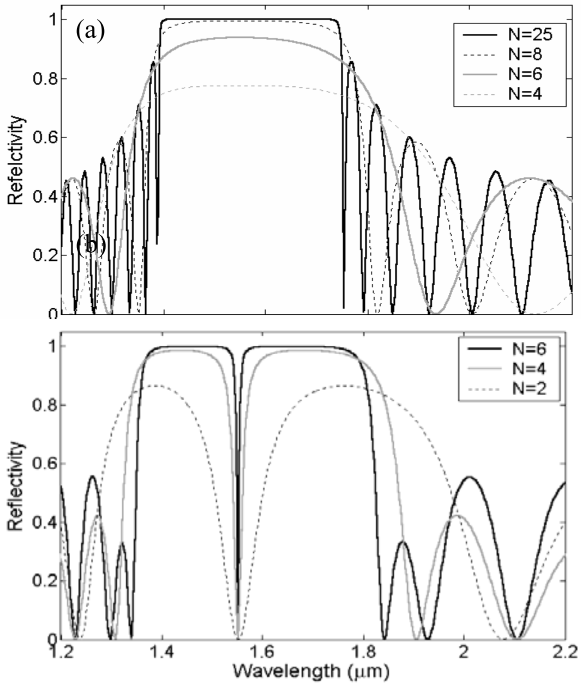

***Fig.2.** Reflectivity spectrum of a multilayer with n_1=2.4, n_2=1.7, h_1=161.6 nm and h_2=228 nm, used as a DBR for λ=1.55 μm (a) and for the formation of a microcavity composed of two symmetric DBR with a defect layer nd=1.35 and hd=575 nm.*

Some omnidirectional mirrors applications are waveguides and substrates for antennas.

7. Conclusions

Porous silicon multilayer structures have been described. We have demonstrated that the optical response of multilayer structures are determined by the refractive index and the thickness of the layers and by the number of periods of the structure. These multilayers have many applications: dichroic Bragg reflectors, microcavities, omnidirectional mirrors, etc. Moreover, the porous microstructure of the material allows infiltration of active media or liquid crystals, which opens many interesting applications of these structures for switching and electrically controlled band-pass filters.

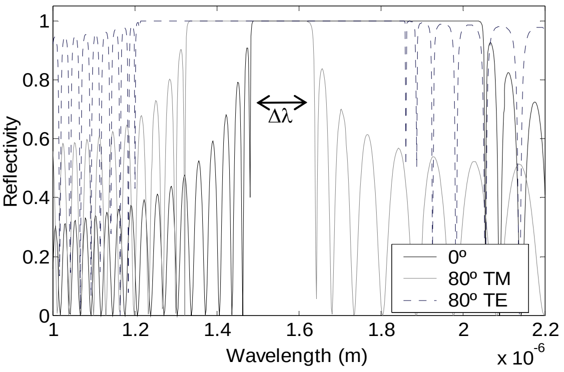

Fig.3. Reflectivity spectra of an omnidirectional mirror with n1=2.5, n2=1.55, h1=176 nm and h2=264 nm for TM and TE polarization and for angles of incidence of 0 and 80 degrees. The omnidirectional bandgap is centered at 1.55 mm (Δλ=102 nm)

References

[1] A.G. Cullis, L.T. Canham, P.D.J. Calcott "The structural and luminescence properties of porous silicon" *J. Appl. Phys.* vol. 82, pp. 909-965, Aug. 1997.

[2] A. Bruyant, G. Lérondel, P. J. Reece, and M. Gal. "All-silicon omnidirectional mirrors based on one-dimensional photonic crystals" *Appl. Phys. Lett.* vol. 82 (19), pp. 3227-3229, May 2003.

[3] P. Yeh, "Optical Waves in Layered Media", Wiley, New York, chap. 5 and 6, 1988.

[4] J. Diener, N. Künzner, D. Kovalev, E. Gross, V.Y. Timoshenko, G. Polisski, F. Koch, "Dichroic Bragg reflectors based on birefringent porous silicon", *Appl. Phys. Lett.* vol. 78 (24), pp.3887-3889, June 2001.

[5] M. Ghulinyan, C.J. Oton, G. Bonetti, Z. Gaburro, L. Pavesi, "Free-standing porous silicon single and multiple optical cavities" *J. Appl. Phys.* vol. 93 (12) pp. 9724-9729, June 2003.

[6] Y. Fink, J.N. Winn, S. Fan, C. Chen, J. Michel, J.D. Joannopoulos, E.L. Thomas "A dielectric omnidirectional reflector" *Science,* vol. 282 pp. 1679-1682, Nov. 1998.